

ABSTRACT

Title of Document: WIND DRIVEN CIRCULATION DYNAMICS
AND SALT BALANCE IN A WIDE
SHALLOW LAGOONAL ESTUARY

Peng Jia, Master of Science, 2011

Directed By: Dr. Ming Li, Professor
Marine, Estuarine and Environmental Sciences

The circulation and salt balance in the Albemarle-Pamlico Sound (APS) are investigated using a 3D hydrodynamic model. Although stratification is weak, the mean flow features a two-layer gravitational circulation. At the seasonal time scale, the circulation is driven by seasonally shifting prevailing winds but also affected by the horizontal density gradients generated by geographically separated sources of freshwater and saline water. The wind-driven circulation in the northern Pamlico Sound shows a laterally sheared flow and is determined by the balance between wind stress and barotropic pressure gradient. In contrast, the circulation in the southern basin shows a vertically sheared flow and is affected by both barotropic and baroclinic pressure gradients. The salt budget in APS is controlled by river flows and salt exchanges through the inlets. The salt flux due to estuarine shear flows is much weaker than that due to tidal pumping and subtidal wind-driven barotropic transport.

WIND DRIVEN CIRCULATION DYNAMICS AND SALT BALANCE IN A
WIDE SHALLOW LAGOONAL ESTUARY

By

Peng Jia

Thesis submitted to the Faculty of the Graduate School of the
University of Maryland, College Park, in partial fulfillment
of the requirements for the degree of
Master of Science
2011

Advisory Committee:
Professor Ming Li, Chair
Professor William Boicourt
Professor Shenn-Yu Chao

© Copyright by
Peng Jia
2011

Acknowledgements

I would like to thank my advisor, Dr. Ming Li, for all his support, both personal and financial, throughout my graduate years. His enthusiasm about my work and research, his willingness to discuss and share ideas, and his dedication to my education made my graduate experience in the US full and successful. I would also like to thank Dr. William Biocourt for his dedication to my papers and research and Dr. Shenn-Yu Chao for providing import insight into the physical processes that were at the core of my thesis. I greatly appreciate their contributions.

I thank Yun Li for helpful discussions. Yonghui Gao, Ji Li, Shuang Li, Yahao Liu and Dakui Wang were the most enjoyable people to work with, and I am thankful for all their support and help throughout the years. I would also thank Dong Yoon Lee, Kevin Meyer, Jeremy Testa, and Jake Goodwin who brought me a colorful life in the US. Patricia Dekker, Deb Morrin-Nordlund, and Brenda Cephas were the most helpful people who made my first year oversea possible. In addition, Hans Paerl was vital to the thesis by providing us with the monitoring data collected by the FerryMon Program.

Last, but not least, I would like to thank my family for their love and fully support, as well as the Horn Point community, who I will miss terribly after I go back to China. I will end with Xin Miao, whose patience and belief in me was amazing throughout my time in graduate school.

Table of Contents

Acknowledgements.....	ii
Table of Contents.....	iii
List of Figures.....	iv
Chapter 1: Background and introduction.....	1
Chapter 2: Model configuration and validation.....	9
2.1. Model configuration.....	9
2.2. Model validation.....	12
Chapter 3: Circulation dynamics in APS.....	18
3.1. Annual mean circulation.....	18
3.2. Dynamics of wind-driven circulation in a wide lagoonal estuary.....	23
3.2.1. Circulation patterns under constant wind forcing.....	24
3.2.2. Momentum balance and vorticity dynamics.....	31
3.3. Seasonal evolution of circulation.....	34
Chapter 4: Wind's effect on stratification.....	56
4.1. Wind straining and mixing effects.....	56
4.2. Semi-durnal Seiching.....	57
4.3. Effects of fresh water input on stratification.....	59
Chapter 5: Salt budget and salt balance.....	70
5.1. Annual Salt Balance.....	71
5.2. Salt flux mechanisms.....	74
5.2.1. Tidal pumping.....	74
5.2.2. Wind driven barotropic salt exchanges.....	77
Chapter 6: Final conclusion.....	91
Bibliography.....	94

List of Figures

Figure 1.1 (a) Map of Albemarle-Pamlico Sound (APS): Chowan, Roanoke, Pamlico and Neuse Rivers discharge freshwater into APS while oceanic water enters it through Oregon, Hatteras and Ocracoke Inlets at the Outer Banks. Model-data comparisons of salinity are conducted along two ferry routes (blue and green lines) and at three stations (black open circles). (b) The rectangular model domain and bathymetry. The black dashed line indicates the location of Bluff Shoal which divides the Pamlico Sound into the southern and northern parts. Open triangles show locations across the three inlets used for the water-level analysis. 8

Figure 2.1 The statistics of wind direction (a) and wind speed (b) in 2003. Discharges from (c) Chowan (dotted) and Roanoke (solid) Rivers, (d) Pamlico (dotted) and Neuse (solid) Rivers during 2003. (e) Weekly mean wind speed vector at a central location in APS. 15

Figure 2.2 Comparison of model-predicted (grey lines) and observed (open circles) salinity time series at (a) station #1 close to the mouth of Pamlico River, (b) station #2 near Ocracoke Inlet, and (c) station #3 in the lower Neuse River. 16

Figure 2.3 Comparisons of model-predicted (black lines) and observed (grey lines) salinity distributions along the northern FerryMon route [blue line shown in Fig. 1.1a] on day 121 (a) with weak horizontal salinity gradient and on day 192 (b) with strong horizontal salinity gradient. Distance is measured from the Ocracoke end of the FerryMon route. 17

Figure 3.1 Mean salinity (in psu) distribution at the surface of APS. (b) Distribution of mean bottom-to-top salinity difference. 40

Figure 3.2 Mean circulation patterns at the (a) surface and (b) bottom of APS. 41

Figure 3.3 Distributions of (a) mean sea level (cm), (b) hydrostatic pressure (Pa) at 3-m depth, and (c) mean wind speed vectors (ms^{-1}) over APS. 42

Figure 3.4 Distributions of depth-integrated (a) barotropic and (b) pressure gradient, (c) surface stress, (d) bottom stress, depth-integrated (e) Coriolis force and (f) nonlinear advection in the southern Pamlico Sound, all in the direction indicated by the arrow in (a). They are in the unit of m^2s^{-2} and multiplied by 10^{-6} 43

Figure 3.5 Mean circulation pattern under constant northeastward wind. Distributions of seasonal mean (a) sea level, (b), depth averaged (c) surface and (d) bottom currents. 44

Figure 3.6 (a) surface and (b) bottom currents under constant southwestward wind; (c) surface and (d) bottom currents under constant southeastward wind.....	45
Figure 3.7 Distributions of cross-section [S1 and N1 in Fig.1.1a] (a) and (b) currents (in 10^{-2} ms^{-1}), (c) Distribution of Ekman number in northeastward wind case.....	46
Figure 3.8 Wind straining vs wind mixing effect. Distributions of currents and salinity on the two along-channel sections [S2 and N2 in Fig.1.1a] (a) and (d) during northeastward wind events, (b) and (e) during southwestward wind events, and the corresponding Wedderburn numbers.....	47
Figure 3.9 Distributions of depth-integrated (a) barotropic and (b) baroclinic pressure gradient, (c) surface stress, (d) bottom stress, (e) Coriolis force and (f) nonlinear advection in the southern Pamlico Sound under northeastward wind, all in the direction indicated by the arrow in (a). They are in the unit of m^2s^{-2} and multiplied by 10^{-6}	48
Figure 3.10 Distributions of depth-integrated (a) barotropic and (b) baroclinic pressure gradient, (c) surface stress, (d) bottom stress, (e) Coriolis force and (f) nonlinear advection in the northern Pamlico Sound under northeastward wind, all in the direction indicated by the arrow in (a). They are in the unit of m^2s^{-2} and multiplied by 10^{-6}	49
Figure 3.11 Distributions of vorticity in 10^{-5} s^{-1} (a) during northeastward wind events, (b) without wind, (c) during southeastward wind events.....	50
Figure 3.12 Distributions of PV balance terms in 10^{-10} s^{-2} under northeastward and southeastward wind conditions: (a) and (c) wind stress curl, (b) and (d) bottom stress curl.	51
Figure 3.13 Mean circulation pattern during spring. (a) Frequency distributions of wind directions. Distributions of seasonal mean (b) sea level, (c) surface and (d) bottom currents.	52
Figure 3.14 Mean circulation pattern during summer. (a) Frequency distributions of wind directions. Distributions of seasonal mean (b) sea level, (c) surface and (d) bottom currents.	53
Figure 3.15 Mean circulation pattern during fall. (a) Frequency distributions of wind directions. Distributions of seasonal mean (b) sea level, (c) surface and (d) bottom currents.....	54
Figure 3.16 Mean circulation pattern during winter. (a) Frequency distributions of wind directions. Distributions of seasonal mean (b) sea level, (c) surface and (d) bottom currents.	55

Figure 4.1 Basinwide mean N^2 in Pamlico Sound under 5 and 10 ms^{-1} wind condition. 1 to 4 stand for four prevailing directions.....	63
Figure 4.2 (a) Time series of total volume (grey) in APS, integrated volume flux (open circles) including river flows, precipitation minus evaporation (P-E) and transports through the inlets, and integrated volume flux (triangles) including river flows and inlet transports only. Time series of (b) total discharges from the four rivers and (c) net precipitation minus evaporation integrated over the surface of APS.	64
Figure 4.3 Discharges from (a) Chowan (dotted) and Roanoke (solid) Rivers, (b) Pamlico (dotted) and Neuse (solid) Rivers in 1999. (c) Weekly mean wind speed vector at a central location in APS.....	65
Figure 4.4 (a) Comparisons of both surface and bottom salinity, and (b) comparison of vertical salinity difference, between observations and the model simulation.	66
Figure 4.5 Distributions of mean (a) surface salinity, (b) vertical salinity difference two weeks before Hurricane Floyd.	67
Figure 4.6 Distributions of mean (a) surface salinity, (b) vertical salinity difference in October 1999.....	68
Figure 4.7 Distributions of mean (a) surface currents, (b) bottom currents in October 1999.....	69
Figure 5.1 Monthly mean surface salinity distributions in (a) February, (b) May, (c) August, and (d) November.....	82
Figure 5.2 (a) Time series of total salt content in APS (thick grey line) and integrated salt flux through all inlets (open circles). (b) Monthly averages of total salt flux through the inlets.....	83
Figure 5.3 Salt flux decomposition at Hatteras Inlet: shear dispersion due to baroclinic exchange flow F_E (dashed line), tidal pumping F_T (black line), and wind-driven barotropic transport F_0 (grey line).	84
Figure 5.4 (a) Time series of sea level at Duck tidal gauge station. Time series of F_T at (b) Ocracoke, (c) Hatteras, and (d) Oregon Inlet.	85
Figure 5.5 Time series of (a) tidal velocity (black) and tidal salinity (green), and (b) the product of tidal velocity and tidal salinity (blue) at Oregon Inlet. Snapshots of depth-averaged velocity (vectors) and salinity (contours) distributions near Oregon Inlet on (c)/(e) peak flood (day 222/229.75) and (d)/(f) peak ebb (day 222.25/230) during the spring/neap tide. The shaded areas are discretized model representations of Outer Banks while the thick solid lines are high-resolution coastlines obtained from NOAA.	86

Figure 5.6 Time series of (a) integrated horizontal advection in the control volume [defined as the quadrilateral marked by red lines in (b)]. Distributions of (b)/(d) vertical salinity difference, (c)/(e) depth-averaged horizontal salinity advection term (in 10^{-4} psu s^{-1}), and (d)/(f) depth-averaged vertical diffusion term (in 10^{-3} psu ms^{-1}) on day 222 (flood) and 222.25 (ebb). 87

Figure 5.7 (a) Wind speed vectors at Cape Hatteras. Time series of subtidal sea levels across (b) Ocracoke, (c) Hatteras, and (d) Oregon Inlet: red dashed lines correspond to stations inside APS and green lines to stations outside APS. Time series of the sectionally averaged barotropic current at (e) Ocracoke, (f) Hatteras and (g) Oregon Inlet. Time series of barotropic salt flux F_0 at (h) Ocracoke, (i) Hatteras and (j) Oregon Inlet. The two days marked in magenta open circles are used in the subsequent analysis. 88

Figure 5.8 Distributions of (a)/(c) subtidal sea level and (b)/(d) depth-averaged subtidal currents (arrows) and salinity (contours) near Oregon Inlet on day 312.5/316.125. Solid arrows in (a) and (c) indicate the wind directions. 89

Figure 5.9 Horizontal distributions of (a)/(d) pressure gradient, (b)/(e) horizontal advection, (c)/(f) bottom stress near Oregon Inlet on day 312.5/316.125. 90

Chapter 1: Background and introduction

Estuaries are semi-enclosed coastal water bodies which receive freshwater from land drainage (Pritchard, 1967). They feature a wide range of topographic shapes, including coastal plain estuaries, fjords, and lagoonal/bar-built estuaries. Much progress has been made in understanding the tidally averaged circulation and stratification in estuaries (MacCready and Geyer, 2010). Width- and tidally averaged momentum and salt equations have been developed to investigate estuarine dynamics (Hansen and Rattray, 1965; Chatwin, 1976) and have led to a greater appreciation of the key role played by the time dependency of the length of the salt intrusion (MacCready, 2004; 2007). In the mean time, advances have been made in understanding detailed dynamics within the tidal cycle and across irregular channel cross-sections (e.g. Simpson et al., 1990; Stacey et al., 1999; Geyer et al., 2000; Valle-Levinson et al., 2000; Lerczak and Geyer, 2006; Scully et al., 2009).

Most of the previous research in estuarine dynamics has focused on the effects of tides. Relatively little attention has been paid to the role of winds in estuarine circulation, despite predictions of first-order effects (Bowden, 1953; Rattray and Hansen, 1962) and observational evidence of strong wind driven flows (e.g., Wang, 1979a, b; Goodrich et al., 1987; Wong and Moses-Hall, 1998; Wong and Valle-Levinson, 2002; Winant, 2004). It has long been recognized that the wind-driven circulation in semi-enclosed estuaries depends on many factors, including wind-stress magnitude and direction, bathymetry, Earth's rotation, density stratification, and

bottom friction. Csanady (1973) analytically solved for wind-driven transport in large lakes using a dynamical balance of wind stress, an opposing sea level gradient, and bottom stress. This work was later expanded (e.g. Hunter and Hearn, 1987; Mathieu et al, 2002) and extended to estuaries (Wong, 1994). Winant (2004) presented an analytic model that includes the previously neglected Coriolis effects. In these steady-state models, there is no net volume flux through an estuarine cross-section. In a flat-bottom channel, the downwind flow occupies the surface layer and the upwind flow is below (Heaps, 1984). Pronounced across-estuary depth variations (e.g. shallow flanks with a deep channel) lead to lateral alignment of inflows and outflows, with surface-intensified downwind jets along the coasts flanking a central bottom-intensified upwind flow over the deepest areas. Wind-driven flow patterns consistent with analytic solutions have been observed in some shallow well-mixed estuaries (e.g. Gutierrez de Velasco and Winant, 2004; Valle-Levinson et al, 2004).

Meanwhile, stratification, which affects vertical momentum exchange processes and therefore the circulation, has been widely investigated. The wind has been treated as a source of kinetic energy that promotes mixing. However, Scully (2005) demonstrated that the along-channel wind plays a dominant role in governing the increase or decrease in vertical density stratification and the corresponding estuarine exchange flow via wind straining effect on the along-channel estuarine density gradient. Down-estuary (up-estuary) winds enhance (decrease) the tidally-averaged vertical shear, which interacts with the along-channel density gradient to increase (reduce) vertical stratification. So at subtidal time scale, in addition to estuarine

density gradient, the along-channel estuarine flow is also affected by the wind straining as well as direct wind mixing.

Additionally, in a shallow and wide system, the friction from bottom boundary layer and the Earth rotation effect have been shown important (Valle-Levinson, 2007). Basin's width, friction, and Earth's rotation are used to determine the conditions under which the density induced exchange flow is vertically sheared or laterally sheared.

Since horizontal density gradient is the key factor for the estuarine response to wind forcing, the salt exchange processes at the estuary mouth and the redistribution of salt inside the estuary have also been intensively studied. The salinity intrusion in an estuary is maintained by a competition between two opposing longitudinal salt fluxes—an advective flux resulting from freshwater outflow, tending to drive salt out of the estuary; and a downgradient salt flux, tending to drive salt landward. Determining the mechanisms that drive the downgradient salt flux in different estuarine classes is a fundamental objective in estuarine research. Both circulation models and measurements have been made to study the tidal as well as subtidal flows and material exchange processes (Churchill et al., 1999; Luettich et al., 1999; Brown et al., 2000; Hench and Luettich, 2003; Vennell, 2006; Waterhouse and Valle-Levinson, 2010). By using observations in the Hudson River estuary, Lerczak and Geyer (2006) studied the salt balance and determined the mechanisms that drive the landward salt flux. Vertical shear dispersion was found to be the dominant

mechanism driving the downgradient salt flux while tidal oscillatory salt dispersion is negligibly low. However, tidal oscillatory salt flux has been found dominant at certain localities where topography changes sharply (Stommel and Farmer, 1952; Wong, 1991; Geyer and Signell, 1992).

Most of the previous studies in estuarine dynamics focus on narrow and long estuaries, such as the James River (e.g. Pritchard, 1955; 1956), Hudson River (e.g. Geyer et al., 2000; Peters, 1999) and Columbia River (e.g. MacCready et al., 2009; Jay and Smith, 1990). Few studies have been devoted to wide and shallow lagoonal estuarine systems having restricted connection to the open ocean through narrow inlets (e.g. Noble et al., 1996; Smith, 2001; Huang et al., 2002). These systems are found on all continents and compose about 13% of the world coastline (Cromwell, 1973). Previous investigations of lagoonal systems have mainly focused on tidal- and wind-driven exchanges across the inlets (Stommel and Farmer, 1952; Wong, 1991; Geyer and Signell, 1992; Churchill et al., 1999; Luettich et al., 1999; Hench and Luettich, 2002; Hench et al., 2003). No comprehensive investigations have been conducted regarding the circulation dynamics inside the lagoonal estuaries.

Albemarle-Pamlico Sounds (APS hereafter) is the largest coastal lagoonal estuary in the United States (Fig. 1.1a). Little attention has paid to its salt balance, stratification and mixing, and circulation. It consists of two major water bodies: Albemarle Sound to the north and Pamlico Sound to the south. Pamlico Sound has two pronounced basins (southern and northern basins) separated by the shallow Bluff

Shoals. Croatan and Roanoke Sounds are two shallow narrow waterways connecting Albemarle and Pamlico Sounds. Compared with its broadness, APS is shallow with an averaged depth of 4.5 m, varying from <2 m on the shoals to over 7.5 m in the center of Pamlico Sound. Neuse and Pamlico Rivers drain into Pamlico Sound while Chowan River and Roanoke River drain into Albemarle Sound. The North Carolina Outer Banks separate APS from the Atlantic Ocean, with three major inlets (Ocracoke, Hatteras and Oregon Inlets) serving as the main passage of saline oceanic water into the estuary (Pietrafesa et al., 1986; Lin et al., 2007).

Previous studies have indicated that the circulation in APS is primarily wind driven (Pietrafesa et al. 1986). Xie and Pietrafesa (1999) developed a 3D baroclinic model for APS (based on the Princeton Ocean Model), and examined APS' response to a sudden shift of wind direction from southwesterly to northwesterly. Xie and Eggleston (1999) used the model to investigate how the circulation and salinity distribution in APS respond to idealized winds in eight different directions. In another modeling study, Luettich et al. (2002) found that winds generate 13.2-h seiching within APS and Neuse River estuary.

Several questions concerning the circulation and salt balance of APS remain unanswered. While it is well known that the stratification is weak in APS, the nature and spatial pattern of the mean circulation are not known. Although baroclinic forcing has been suggested to play a role in APS (Pietrafesa et al., 1986), it is unclear if the mean circulation is driven by the winds or by the gravitational force created by geographically separated sources of freshwater (rivers) and salty water (inlets).

Previous modeling studies have shown that winds are the major mechanism driving the circulation in APS at short time scales (daily to weekly). On the seasonal scale, winds over APS shift from southeastward winds during winter to northeastward winds during summer. How does the seasonal shift of prevailing winds affect the circulation pattern? Since APS is representative of a class of shallow and wide lagoonal estuaries, understanding its circulation dynamics has wide implications. APS generally lacks stratification which, however, varies dramatically from time to time. How does the seasonal shift of prevailing winds affect the stratification? How does fresh water input which brings large amount of buoyancy affect the stratification? APS receives freshwater from four rivers and exchanges salt with the Atlantic Ocean through the three inlets. How do the river flows and salt fluxes through the inlets affect the seasonal evolution of salinity distribution in APS? What is the contribution of the wind-driven flows to the salt flux into APS?

In this study we conduct hindcast simulations of APS estuary using year 2003 and year 1999 as examples. Our objectives are three-fold: (1) to examine the flow response to winds in characteristic wind directions and investigate the short time scale to seasonal- mean circulation patterns and seek their driving mechanisms; (2) to study the effects of wind and fresh water input on stratification; (3) to determine the major driving mechanisms that influence the salt exchange of APS. In Chapter 2, we introduce the ROMS model for APS and describe the validation of model results against observations. Chapter 3 is devoted to the analysis of three idealized cases and wind driven circulation in this wide and shallow lagoonal estuary. Chapter 4 is

devoted to determine the effects of wind and fresh water input on stratification. In Chapter 5, analysis of salt flux through inlets and salt balance in the whole system is conducted. Concluding remarks are made in Chapter 6.

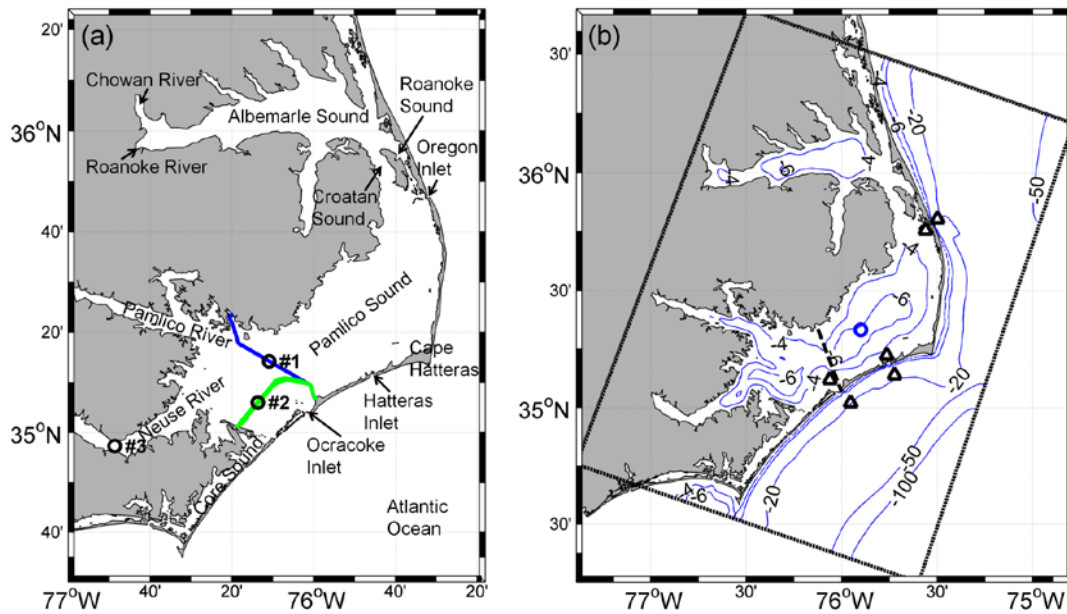


Figure 1.1 (a) Map of Albemarle-Pamlico Sound (APS): Chowan, Roanoke, Pamlico and Neuse Rivers discharge freshwater into APS while oceanic water enters it through Oregon, Hatteras and Ocracoke Inlets at the Outer Banks. Model-data comparisons of salinity are conducted along two ferry routes (blue and green lines) and at three stations (black open circles). (b) The rectangular model domain and bathymetry. The black dashed line indicates the location of Bluff Shoal which divides Pamlico Sound into the southern and northern parts. Open triangles show locations across the three inlets used for the water-level analysis.

Chapter 2: Model configuration and validation

To answer those questions raised in Chapter 1, we develop a 3D hydrodynamic model for APS using ROMS (Regional Ocean Modeling System; Haidvogel et al., 2000). ROMS is a hydrostatic, primitive equation model using a curvilinear/rectangular grid in the horizontal directions and a stretched, terrain-following coordinate in the vertical direction (Song and Haidvogel, 1994). It has been successfully applied to several estuaries, including the Hudson River estuary (Warner et al., 2005a), Chesapeake Bay (Li et al., 2005; Li and Zhong, 2009), Columbia River and Oregon shelf (MacCready et al., 2009), and Puget Sound (Sutherland et al., 2010).

2.1. Model configuration

Bathymetry is extracted from high-resolution Coastal Relief Model data archived at NOAA's National Geophysical Data Center. The model domain covers Albemarle Sound, Pamlico Sound, four major tributaries (Neuse River, Pamlico River, Chowan River and Roanoke River), and a part of the coastal ocean to facilitate free exchange between the estuary and adjacent shelf (Fig. 1.1b). Coastal boundaries are specified as a finite-discretized grid via land/sea masking. The total number of grid points is 142x162. The grid spacing is about 1.4 km in most places, but finer resolution (about 200 m) is placed inside the three inlets that connect APS to the Atlantic Ocean (8x2 grid points in each inlet). The model has 20 vertical layers. A quadratic stress is exerted at the bed, assuming that the bottom boundary layer is logarithmic over a

roughness height of 1 mm (Reyns et al., 2006; Xu et al., 2008). The vertical eddy viscosity and diffusivity are computed using the k - kl turbulence mixing scheme with the background viscosity and diffusivity at $10^{-5} \text{ m}^2\text{s}^{-1}$ (Warner et al. 2005b). Coefficients of the horizontal eddy viscosity and diffusivity are set to $1 \text{ m}^2\text{s}^{-1}$.

The model is forced by freshwater inflows at river heads, tidal and non-tidal flows at the offshore boundary, and winds, heat and freshwater exchanges across the water surface. At the upstream boundary in the four tributaries, daily freshwater inflows with zero salinity and time-varying temperature are prescribed. The river flows obtained at USGS gauging stations are multiplied by the ratio of the entire river's drainage to the drainage area of the monitoring station (Lin et al., 2007). Figures 2.1c and d show the time series of river flows in 2003: Chowan and Roanoke Rivers which drain into Albemarle Sound; Neuse and Pamlico Rivers which drain into Pamlico Sound.

At the offshore open boundary, the condition for the barotropic component consists of a Chapman's condition for surface elevation and a Flather's condition for barotropic velocity. The boundary condition for the baroclinic component includes an Orlanski-type radiation condition for baroclinic velocity and a combination of radiation condition and nudging (with a relaxation timescale of 1 day) for temperature and salinity (Marchesiello et al., 2001). Tidal forcing at the open ocean boundary is decomposed into ten constituents (M_2 , S_2 , N_2 , K_2 , K_1 , O_1 , P_1 , Q_1 , M_f , M_m) using the harmonic constants linearly interpolated from Oregon State University global inverse tidal model of TPXO7 (Egbert et al., 1994; Egbert and Erofeeva, 2002). For non-tidal

forcing at the open-ocean boundary, we use monthly sea levels constructed from Simple Ocean Data Assimilation (SODA) (Carton et al., 2000a; b). De-tided daily sea-level observations acquired at NOAA Duck and Beaufort stations are added to the monthly SODA boundary conditions at the northern and southern boundaries, respectively. The baroclinic velocity is prescribed using the monthly data from SODA. The salinity and temperature fields at the open boundary are obtained from monthly Levitus climatology (Levitus, 1982).

Air-sea fluxes of momentum, heat and freshwater across the surface of APS are computed by applying standard bulk formulae (Fairall et al., 2003) to NARR (North America Regional Reanalysis from National Center for Environmental Prediction) products (Mesinger et al., 2004). Hourly winds are interpolated from NARR 3-hour winds and have been validated against observations at 14 weather stations scattered across APS (see www.wunderground.com). Figure 2.1e shows weekly mean wind vectors in 2003. Southeastward winds dominate during the winter whereas winds are predominately northeastward during the summer. Wind directions are variable during the spring and fall transition periods.

Given APS' wide surface area, local precipitation (P) and evaporation (E) may affect salinity concentrations inside the sound. High resolution P and E are also from NARR 2003. Although throughout a whole year local P and E are nearly cancelled out, large seasonal fluctuations happen.

We conducted hindcast simulation for both 2003 and 1999. To initialize the model for 2003 (1999), we ran the model for 2002 (1998) using the observed forcing data. Model outputs at the end of 2002 (1998) were used to set the initial condition for the salinity and temperature fields. The initial velocity field was taken to be zero, and the water surface was set at the mean sea level.

As simplified scenarios of the realistic, idealized numerical experiments are conducted to unveil the fundamental mechanisms driving circulation dynamics in APS. Three sets of idealized winds with persistent speed and direction, mimicking the seasonal prevailing winds, are used to drive the model for idealized numerical experiments. The three dominant wind directions are northeastward, southwestward and southeastward indicated by the statistics of annual wind direction of year 2003 (Fig. 2.1a). The wind speeds are set to 5ms^{-1} (Xie et.al., 1999). Speed histograms lead to the confirmation of this typical speed (Fig. 2.1b). They are applied to the model from the annual mean condition of 2003 simulation. To ease analysis, all the other forces including tides, rivers and precipitation rate as well as offshore boundary conditions are annually averaged and then used to drive the model until steady states.

2.2. Model validation

The model results from 2003 simulation have been validated against salinity measurements acquired by the Ferry Monitoring program (FerryMon hereafter). The state of North Carolina uses the Department of Transportation Ferry Service to record water-quality parameters (such as salinity) aboard ferry boats (Buzzelli et al., 2003; Paerl et al., 2009). Two routes span across Pamlico Sound, connecting the Outer bank

posts to the mainland locations, as shown in Fig. 1.1a. The salinity data collected from FerryMon were processed for quality control according to NDBC's (National Data Buoy Center) standard procedures (NDBC Technical Document 09-02). Three stations (marked in Fig. 1.1a) were selected for comparing the salinity time series (Fig. 2.2). They occupy different salinity regimes: Station #1 lies half way between the mouth of Pamlico River and Ocracoke Inlet; Station #2 is located in southern Pamlico Sound; and Station #3 is in the lower Neuse River. Due to operational constraints of ferry boats and applications of data-quality control, the observational data were sparse during some periods. Nevertheless, there are reasonable agreements between the observed and modeled salinity time series. In particular, the model captures spring freshening at Station #1 really well. It also reasonably reproduces the seasonal variation at Station #2, although the model overpredicts salinity in the later half of the year. At Station #3, the few available data points fall onto the modeled salinity time series.

We have also used the FerryMon data to test model predictions for the horizontal salinity distribution (Fig. 2.3). The ferry route between Ocracoke Inlet and Swan Quarter (marked as the blue line in Fig. 1.1a) connects Pamlico River to the Outer Bank. Since ferries traveled back and forth several times in a day, multiple lines of observed salinity were shown. As a preliminary comparison, we plotted the model-predicted salinity distribution at noon. There are reasonable model-data agreements during the two days with contrasting conditions: the horizontal salinity gradient was relatively weak on day 121 but very strong on day 192.

In addition to the salinity comparison, we compared the model-predicted subtidal sea-level fluctuations against observations near tidal gauges inside and outside APS: NOAA station at Duck, North Carolina; USGS station at Washington, North Carolina in Pamlico River; and USGS station Fort Barnwell, North Carolina in Neuse River. There are very good agreements on the predicted and observed sea level at the three stations (figure not shown). The correlation coefficient is 0.98 and the root mean square error is 5 cm.

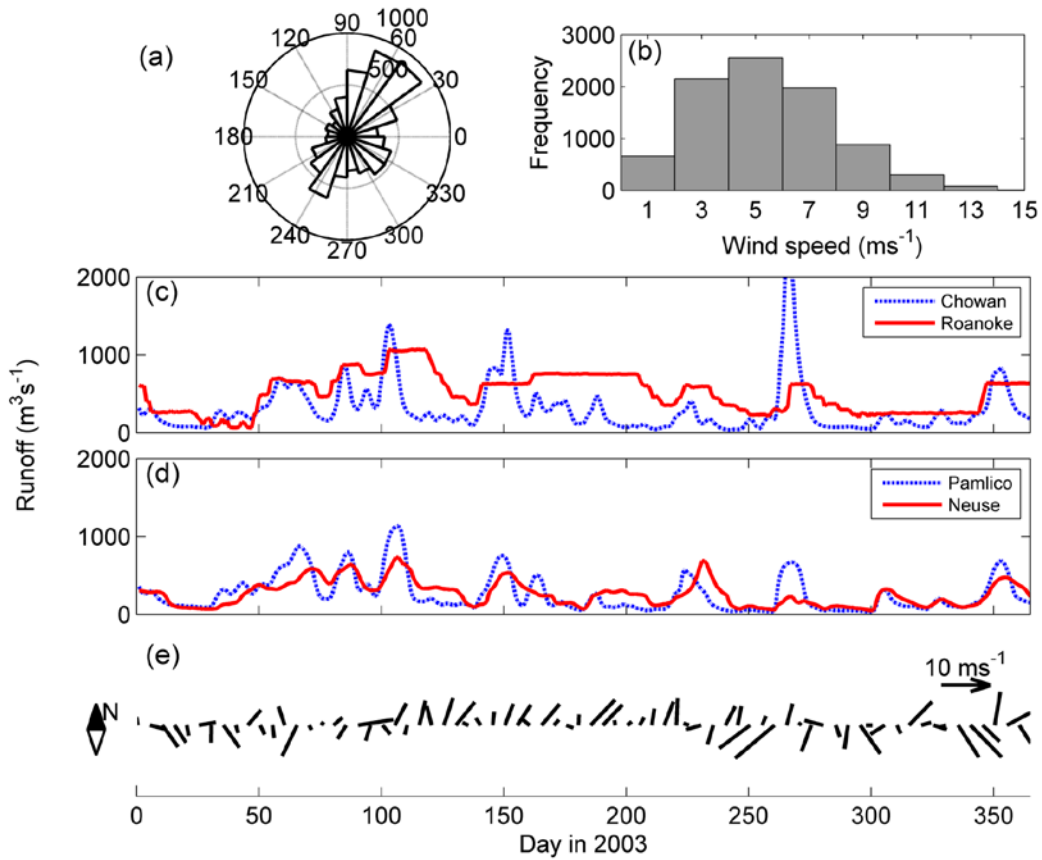


Figure 2.1 The statistics of wind direction (a) and wind speed (b) in 2003. Discharges from (c) Chowan (dotted) and Roanoke (solid) Rivers, (d) Pamlico (dotted) and Neuse (solid) Rivers during 2003. (e) Weekly mean wind speed vector at a central location in APS.

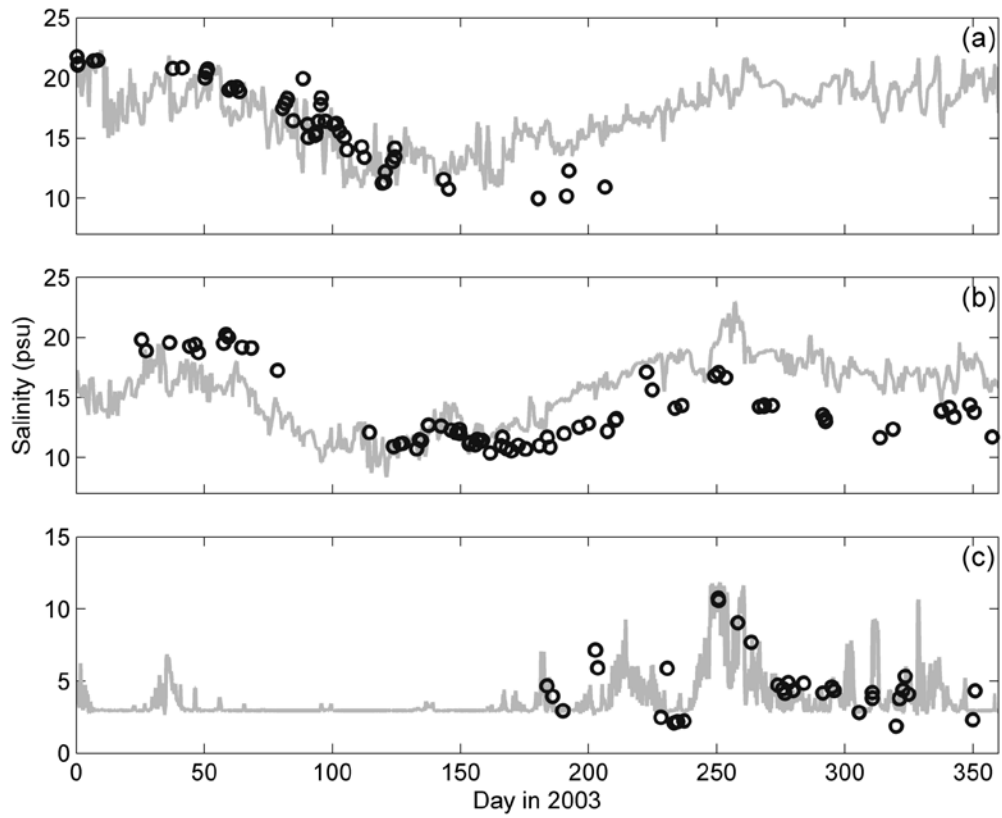


Figure 2.2 Comparison of model-predicted (grey lines) and observed (open circles) salinity time series at (a) station #1 close to the mouth of Pamlico River, (b) station #2 near Ocracoke Inlet, and (c) station #3 in the lower Neuse River.

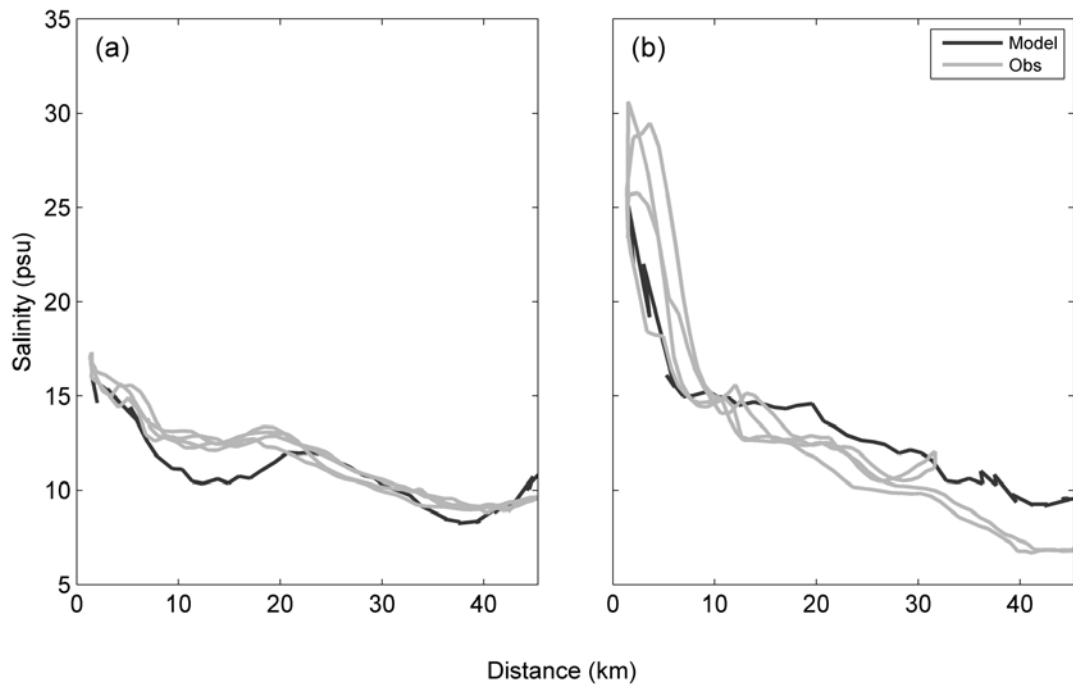


Figure 2.3 Comparisons of model-predicted (black lines) and observed (grey lines) salinity distributions along the northern FerryMon route [blue line shown in Fig. 1.1a] on day 121 (a) with weak horizontal salinity gradient and on day 192 (b) with strong horizontal salinity gradient. Distance is measured from the Ocracoke end of the FerryMon route.

Chapter 3: Circulation dynamics in APS

Csanady (1973) and Winant (2004) analytically solved the wind-driven transport in large lakes, which are then extended to estuaries. Wind-driven flow patterns consistent with analytic solutions have been observed in some shallow well-mixed estuaries (e.g. Gutierrez de Velasco and Winant, 2004; Valle-Levinson et al, 2004). What's the basic circulation pattern in APS? What's the driving mechanism for this mean circulation? How does the wind change this circulation? What's the role the horizontal density gradient playing? To answer these questions, in this chapter we will discuss the mean circulation pattern and its driving forces, the wind-driven circulation and density-driven circulation in APS, and their seasonal evolution.

3.1. Annual mean circulation

Previous investigations have shown that the stratification in APS is weak except in and near the tributaries (e.g. Roelofs and Bumpus, 1953; Pietrafesa et al., 1986). However, the mean circulation pattern in this weakly stratified estuary is not well known. It is not clear if the circulation is driven by the winds or by the horizontal density gradients set up by geographically separated freshwater (rivers) and saltwater sources (inlets). In this section we investigate the dynamics of the mean circulation and seek for its driving mechanism.

To begin with, we plot the annual-mean surface salinity distribution in Fig. 3.1a. Albemarle Sound receives freshwater from Chowan and Roanoke Rivers and does not

have direct exchanges with the Atlantic Ocean. Hence salinity in Albemarle Sound is low (less than 1 psu) but increases sharply across narrow Croatan and Roanoke Sounds. In contrast, salinity is much higher in Pamlico Sound since three major inlets, Oregon, Ocracoke, and Hatteras, connect it to the Atlantic Ocean. Not surprisingly, highest salinities are found close to the inlets. The 13-psu isohaline reaches as far inland as the mouths of Neuse and Pamlico Rivers. Salinity distribution in Pamlico Sound reveals two different geographic patterns. The salinity gradient is aligned in the east-west direction in southern Pamlico Sound (between Neuse-Pamlico Rivers and Outer Bank) since freshwater is discharged from Pamlico and Neuse Rivers. A north-south salinity gradient develops in northern Pamlico Sound (between Croatan Sound and Hatteras Inlet) since low-salinity Albemarle water enters Pamlico Sound at the northern end. As a measure of the vertical stratification, the surface-to-bottom salinity difference is plotted in Fig. 3.1b. The salinity difference is less than 2 psu in most places. Pronounced stratification is only found in Neuse and Pamlico Rivers, near the three inlets at the Outer Bank, and in a part of southern Pamlico Sound where freshwater spread seaward at the surface. As discussed in previous papers (e.g. Luettich et al., 2002), this weak stratification is a result of strong wind-induced mixing over shallow water. The average eddy diffusivity inferred by volume averaging from the model reaches about $2.5 \times 10^{-3} \text{ m}^2 \text{ s}^{-1}$ in APS.

Next we investigate the mean circulation pattern. Figure 3.2 shows the annual-mean current patterns at the surface and bottom of APS. The surface current flows out of Albemarle Sound, with maximum speeds in the narrow Roanoke and Croatan

sounds. This current bifurcates. One branch turns left and exits the Sound through Oregon Inlet. The other branch continues its southward path into Pamlico Sound. Strong surface outflows are also seen to come out of Neuse and Pamlico Rivers. A convergence zone develops around Bluff Shoals (see Fig. 1.1b) where the eastward flows from Pamlico and Neuse Rivers meet the southward flows from Albemarle Sound. Over the inner shelf outside the Outer Banks, the flow is directed northward due to the effects of the Gulf Stream and the south-north sea-level pressure gradient established in the South Atlantic Bight (Werner et al., 1993; Werner and Brain, 1999; Savidge and Bane, 2001). Inside APS, the bottom currents generally move in the opposite direction as the surface currents. Westward flows are directed into Pamlico and Neuse Rivers. The bottom water flows northward in the northern half of Pamlico Sound and intrudes into the narrow Roanoke and Croatan sounds. With nearly fresh water, Albemarle Sound behaves like an extended river so that the bottom current moves in the same direction as the surface current. Therefore, despite the weak stratification, APS features a vertically sheared two-layer mean circulation with current speeds reaching several cm s^{-1} .

To understand what drives this two-layer circulation, we plot the sea-level distribution as well as the pressure distribution at 3-m depth (Fig. 3.3). Sea level is highest in Albemarle Sound due to the inflows from Chowan and Roanoke Rivers. It is also high in Neuse and Pamlico Rivers. In comparison, the sea level is relatively low in the middle part of Pamlico Sound. Therefore, a north-south sea-level slope develops in the northern part of Pamlico Sound and a west-east sea-level slope

develops in the southern part of Pamlico Sound. These sea-level slopes can drive a southward surface flow in the northern Pamlico Sound and an eastward surface flow in the southern Pamlico Sound. The pressure at 3-m depth shows a pattern of high and low pressure centers that are opposite to the sea-level distribution (Fig. 3.3b). Since high-salinity Atlantic water enters APS through the inlets at the Outer Banks, the hydrostatic pressure is higher in the central part of Pamlico Sound than that in Albemarle Sound as well as in Neuse and Pamlico Rivers. This horizontal pressure gradient is directed westward in the southern part of Pamlico Sound and northward in the northern part of Pamlico Sound, thus driving the bottom return flows as seen in Fig. 3.2b. In contrast, the annual-mean wind speed is weak and has no apparent correlation with the circulation pattern (Fig. 3.3c).

Further insights into the circulation dynamics can be gained by examining the along-channel momentum equation

$$\frac{\partial u}{\partial t} = -g \frac{\partial \eta}{\partial x} - \frac{g}{\rho} \int_z^{\eta} \frac{\partial \rho'}{\partial x} dz' + \frac{1}{\rho} \frac{\partial \tau_{xz}}{\partial z} + fv - \left\{ u \frac{\partial u}{\partial x} + v \frac{\partial u}{\partial y} + w \frac{\partial u}{\partial z} \right\}. \quad (3.1)$$

We have compared the along-channel pressure gradient $-g \frac{\partial \eta}{\partial x} - \frac{g}{\rho} \int_z^{\eta} \frac{\partial \rho'}{\partial x} dz'$ and

along-channel velocity at two representative cross sections in the southern and northern Pamlico Sounds, respectively (figure not shown). The pressure gradient switches sign between the surface and bottom layers at both sections.

Correspondingly, the circulation shows a vertically sheared two-layer flow pattern.

Integrating (1) from the bottom to the surface and averaging over time leads to

$$\begin{aligned}
0 = & \underbrace{\int_{-h}^{\eta} -g \frac{\partial \eta}{\partial x} dz}_{\text{barotropic pressure gradient}} + \underbrace{\int_{-h}^{\eta} \left\{ -\frac{g}{\rho} \int_z^{\eta} \frac{\partial \rho'}{\partial x} dz' \right\} dz}_{\text{baroclinic pressure gradient}} + \underbrace{\frac{\tau_s}{\rho}}_{\text{surface stress}} - \underbrace{\frac{\tau_b}{\rho}}_{\text{bottom stress}} \\
& + \underbrace{\int_{-h}^{\eta} f v dz}_{\text{Coriolis force}} - \underbrace{\int_{-h}^{\eta} \left\{ u \frac{\partial u}{\partial x} + v \frac{\partial u}{\partial y} + w \frac{\partial u}{\partial z} \right\} dz}_{\text{Advection}} \quad (3.2)
\end{aligned}$$

We analyze this momentum balance in the southern Pamlico Sound, as shown in Fig. 3.4. The two largest terms are the barotropic and baroclinic pressure gradients which are of the opposite sign. The barotropic pressure gradient associated with the river-induced sea level slope points eastward whereas the baroclinic pressure gradient associated with the horizontal salinity gradient points westward. The surface wind stress is significantly smaller than the pressure gradient terms. The bottom stress is even weaker, except near the Ocracoke Inlet where the bottom currents are strong. Both the depth-integrated Coriolis force and nonlinear advection terms are small, although the flow convergence/divergence amplifies the advection term near the Ocracoke Inlet. We have also examined the depth-integrated along-channel momentum balance for the northern Pamlico Sound and found essentially the same result. Hence the momentum balance analysis demonstrates that the gravitational force is the dominant mechanism driving the mean two-layer circulation in the weakly stratified lagoonal estuary of APS.

3.2. Dynamics of wind-driven circulation in a wide lagoonal estuary

In semi-enclosed estuaries, the wind-driven circulation will be influenced by several factors including wind-stress magnitude and direction, bathymetry, Earth's rotation, density stratification, and bottom friction. Figure 1.1b shows the bathymetry in APS. The broad APS is very shallow so that bottom friction and Earth's rotation are expected to be important. Both Albemarle Sound and northern Pamlico Sound show the classic lake bathymetry: a relatively narrow deep channel flanked by wide shallow shoals at the two sides. In comparison, the southern Pamlico Sound shows a wide deep channel and steep sides. Due to these bathymetric differences, different parts of the estuary may respond differently to the same wind forcing.

APS has geographically separated sources of fresh and saline waters. Figure 3.1a shows the mean salinity distribution at the surface of APS. Albemarle Sound has low salinity almost everywhere. Salinity is much higher in Pamlico Sound since three major inlets, Oregon, Ocracoke, and Hatteras, connect it to the Atlantic Ocean. Salinity distribution in Pamlico Sound reveals two different geographic patterns. The salinity gradient is aligned in the east-west direction in southern Pamlico Sound (between Neuse-Pamlico Rivers and Outer Bank) since freshwater is discharged from Pamlico and Neuse Rivers. A north-south salinity gradient develops in northern Pamlico Sound (between Croatan Sound and Hatteras Inlet) since low-salinity Albemarle water enters Pamlico Sound at the northern end. Additionally, APS lacks vertical stratification. The annual mean surface-to-bottom salinity difference is plotted in Fig. 3.1b. The salinity difference is less than 2 psu in most places. A

question is if and how these horizontal density gradients affect the wind-driven circulation in the sound.

To gain new insights into the circulation dynamics in APS, we have conducted process-oriented studies with idealized wind forcing. In the idealized experiments, we fixed the river discharges of the four tributaries at their respective annual averages. From the analysis of long-term measurements of wind speeds at a representative meteorological station (near Cape Hatteras), we found that the winds have a mean speed of 5 ms^{-1} and blow in three dominant directions: southwestward, northeastward and southeastward (Figs. 2.1a and 2.1b). Hence three numerical experiments with the wind-speed magnitude fixed at 5 ms^{-1} and the wind direction pointed in the three dominant directions are conducted. Because of its shallowness, APS responds rapidly to the wind forcing. After the application of idealized winds, APS reaches its quasi-steady state in 10 days. The model results from day 10 to day 15 since the wind deployment are used for the following analysis.

3.2.1. Circulation patterns under constant wind forcing

The summer wind points toward northeast as shown in Fig. 3.5a. Under this strong wind, the sea level is redistributed (Fig. 3.5a). Water from Albemarle Sound is chocked in the eastern end setting up high sea level in that region. From Oregon Inlet to Neuse River, a basin-wide northeast-southwest sea level gradient exists (shown in Fig. 3.5a).

Albemarle Sound and Pamlico northern basin behave more similarly. Fig. 3.5b shows the depth averaged currents. In the shallow portions of both basins, the currents go downwind while in the depth upwind. At any location, both surface and bottom currents follow the same direction (Fig. 3.5c and d). However, two-layer circulation, with seaward surface currents and landward bottom currents, develops in the Pamlico southern basin (Fig. 3.5c and d). Both surface and bottom currents are relatively strong.

Similarly, the responses of three basins to strong winter southwestward wind and southeastward wind are different (Fig. 3.6). The southwestward wind drives strong surface outflows from Albemarle Sound penetrating farther to the south (Fig. 3.6a). In the shallow Outer Banks and west bank, both surface and bottom flows are in the wind direction. In the deep central portion, currents are generally in the opposite direction. In the Pamlico southern basin, two-layer circulation with surface landward and bottom seaward currents occupies the most area (Fig. 3.6a and b).

The southeastward wind also drives strong surface outflows from Albemarle Sound as well as from Pamlico and Neuse Rivers penetrating farther to the east (Fig. 3.6c). Two flow branches originated from Pamlico and Neuse Rivers converge and cross the Pamlico Sound towards the Outer Banks. The bottom currents generally move in the opposite direction to the surface currents (Fig. 3.6d). When the southeastward winds set up a higher sea levels along Bluff Shoal (figure not shown),

this east-west sea level slope works together with the already existing east-west density gradient driving a counter flow at the bottom.

Our focus here is on axial wind effects. Therefore, the wind direction is either up-estuary or down-estuary. The difference between the Pamlico southern and northern basin is the axial wind direction. Because of the alignment of Outer Banks, the summer northeastward wind is mainly up-estuary for the Pamlico northern basin but down-estuary for the Pamlico southern basin because the effective component of the northeastward wind opposes the east-west salinity gradient in the southern basin.

Valle-Levinson (2007) studied the lateral current structure of density-driven exchange flow in an estuary (vertically sheared versus laterally sheared) using theoretical and analytic models based on Ekman and Kelvin numbers. The Ekman number is defined as

$$E_k = \frac{A_z}{fH^2} \quad (3.3)$$

where A_z is the flow's eddy viscosity, f is the Coriolis factor, H is the local water depth. E_k can be interpreted as the square of the ratio of Ekman depth over the water depth.

A basin's width has been traditionally recognized to determine whether Earth's rotation effects on water exchange are appreciable or not (e.g., Pritchard, 1952). If the

basin is wider than the internal Rossby radius R_i , then rotation should be important (e.g., Gill, 1982). In a density induced flow, R_i is given by

$$R_i = \frac{\sqrt{g'h}}{f} \quad (3.4)$$

where h is the depth of the buoyant part of the density induced flow, and f is the Coriolis parameter, g' is the reduced gravity which equals $g\Delta\rho/\rho_0$, g is the gravity acceleration, ρ_0 is a reference water density, and $\Delta\rho$ is the contrast between the buoyant water density and the density underneath. The Kelvin number K_e compares the basin's width B to R_i

$$K_e = \frac{B}{R_i} \quad (3.5)$$

indicating the importance of Earth's rotation effects which are supposed to be most prominent when $K_e > 1$.

The exchange pattern consisting of net inflows in the deep channel and outflows over shoals develops only under high frictional conditions ($E_k > 1$) independently of the basin's width (Valle-Levinson, 2007). This is a laterally sheared exchange pattern which is shown in Fig. 3.7b in the Pamlico northern basin where $E_k > 0.5$ mostly (Fig. 3.7c). The lateral segregation is consistent with Csanady's analytical solution for wind-driven flow over laterally varying bathymetry. The wind-driven circulation in lakes, lagoons, estuaries, or coastal embayments is described with a linear, steady, three-dimensional barotropic model in an elongated basin of arbitrary depth

distribution by Csanady (1973) and Winant (2004). Without rotation, Csanady (1973) has shown that the vertically integrated transport is proportional to total water depth. With rotation, the vertically averaged velocity scales with the Ekman depth rather than the maximum depth as in the case without rotation (Winant, 2004). Since the Ekman number in Pamlico northern basin is very close to 1 (Fig. 3.7c), Csanady and Winant's solutions yield very similar results in our study area. Not surprisingly, under both northeastward and southwestward winds, laterally segregated circulation also develops in Albemarle Sound which also has a high Ekman number and is frictionally controlled.

In contrast, under weak frictional conditions ($E_k \rightarrow 0$), the exchange pattern is laterally sheared in wide basins ($K_e > 2$). The internal Rossby radius of deformation in our system is about 5.5-8km, which is much smaller than the channel width (20-30km). Therefore, the influences of rotation on currents could be significant (e.g., Sanay 2003). In APS, horizontally shared two-layer circulation develops under weak wind condition indicated by the positive vortexes (anti-clockwise) in both Pamlico southern and northern basins (Fig. 3.11b).

As shown in Fig. 3.7c, E_k is smaller in the Pamlico southern basin, suggesting a horizontally sheared two-layer flow under high Kelvin number. However, we see a more vertical shared two-layer flow in the southern basin (Fig. 3.7a). Large buoyancy inputs from the four rivers create stratification and baroclinic effects that modify the wind-event response. Wedderburn number (Monismith 1986), a nondimensional

parameter which shows the relative importance between wind stress and scaled baroclinic pressure gradient force, is introduced here to describe the effects of wind and density gradient on the circulation pattern in APS:

$$W = \frac{L\tau_{wx}}{\Delta\rho gH^2} \quad (3.6)$$

where τ_{wx} is the along-channel wind stress (positive is down-estuary), L is the length of the each basin, $\Delta\rho$ is the density change over L , g is the gravitational acceleration, and H is the averaged depth. Under 0.03 Pa wind (5 m s^{-1}), for the Pamlico northern basin where L is around 50 km with an averaged depth of 4 m and a ΔS (horizontal salinity difference) of 5 psu, the Wedderburn number is around 2.

The Wedderburn number may also be interpreted as the relative strength of wind-driven and gravitational circulations on estuarine residual flows (Geyer 1997). Scully et al. (2005) proposed that in shallow estuaries down-estuary (up-estuary) wind can enhance (reduce) exchange flow (i.e., stratifying subtidal vertical shear) through straining effect on along channel density gradient. However, direct wind mixing favors decreases in exchange flow as wind stress generates a turbulent boundary layer that propagates downward to erode exchange flow. The competition between the two processes determines the wind's effect on density-driven gravitational circulations.

The most effective wind stress for the Pamlico southern basin is roughly in west-east direction. During northeastward wind, this component is 0.2 Pa and down-estuary yielding a Wedderburn number around 0.8 indicating a wind-driven flow as strong as and in the same direction with the density-driven flow. The water column is

more stratified because the tendency toward increasing stratification by wind straining dominates over direct wind mixing (Scully, 2005). Compared with weak-wind condition, N^2 doubles in most region and exchange flow increases from 0.1 to 0.2 m s^{-1} (Fig. 3.8a). However, the southwestward wind which induces a westward wind (up-estuary) tilts the isopycnal reducing the stratification. W is as large as -1.5 indicating wind driven flow overpasses and then reverses density driven flow, so a reversed the two-layer circulation is shown in Fig. 3.8b. If the wind (both down- and up-estuary) keeps increasing up, the surface mixed layer will be deep enough and quickly overcome the wind straining which finally decreases exchange flow.

For the Pamlico northern basin, although the density effect is weak, the Wedderburn number is also helpful to understand the circulation. The currents under both wind conditions are less complicated (Fig. 3.8c and d). The strong northeastward wind (5 m s^{-1}) yields a Wedderburn number around -2.3 indicating that wind-driven axial flow dominates over gravitational circulation. As a result, the current and salinity structures are radically different from those under the non- or weak- wind condition. The northern basin is almost vertically homogenous which favors decreases in stratification and then feeds back to decrease exchange flow through increased vertical momentum exchange. Meanwhile, wind straining which opposes the density gradient also tends to reduce exchange flow farther. This leads to decreasing vertical shear and finally a laterally segregated circulation in the northern basin. As aforementioned, under high Ekman number, the circulation features wind

driven and frictionally controlled so that Csanady's solution applies. In Fig. 3.8d, similar response shows under southwestward wind [$W = 1.7$].

In summary, in the Pamlico northern basin and Albemarle Sound, under both northeastward and southwestward winds, wind-driven axial flow dominates over gravitational circulation [$W \approx \pm 2$]. The Ekman depth roughly equals the total water depth [$E_k \approx 1$]. Under such high frictional condition, laterally segregated circulation develops and is consistent with Csanady's analytical solution for wind-driven flow over laterally varying bathymetry (Fig. 3.8c and d). Density-driven flow is much weaker. However, in the Pamlico southern basin, large horizontal density gradient modulates the flow's response to the wind. During northeastward wind, the vertically exchange flow is strengthened because wind-driven flow and density-driven gravitational circulation are in concert (Fig. 3.8a). During southwestward wind event, the competition between wind-driven and gravitational circulation is evident when the exchange flow decreases and then reverses sign [$W < -1$] (Fig. 3.8b).

3.2.2. Momentum balance and vorticity dynamics

How does Pamlico southern basin respond so differently from the northern basin and Albemarle Sound? Further insights into the circulation dynamics can be gained by examining the along-channel momentum equation (3.2). We first analyze this momentum balance in the southern Pamlico Sound, as shown in Fig. 3.9. The two largest terms are barotropic pressure gradient and surface stress which are of the opposite sign. Nonlinear advection also plays a role in the vicinity of river mouths

and inlets where the flow convergence/divergence amplifies the advection. It is not surprising that friction and rotation are important since surface and bottom currents are both strong in the Pamlico southern basin. It is surprising that two pressure gradients, both barotropic and baroclinic, are of the same sign against the surface stress. An eastward wind component is applied to the southern basin by the northeastward wind. It blows surface water down-estuary opposing the large east-west salinity gradient. Water is piled up around Bluff Shoal by this down-estuary wind. Two-layer circulation is still maintained by the competition between wind stress and total pressure gradient (barotropic plus baroclinic). At the surface where pressure gradient is small, currents follow the direction of surface wind and fresh water from rivers spreads seaward. However, pressure gradient increases with depth and becomes big enough to drive a return flow at the bottom shown in Fig. 3.5a. The current switches sign vertically which depicts perfectly a two-layer flow as shown in Fig. 3.7a. Hence the momentum balance analysis demonstrates that the wind force is a dominant factor driving the circulation. Gravitational force which is in concert with wind strengthens the vertical shear. Additionally, the other factors like earth rotation and friction also play roles in the development of the circulation (Fig. 3.9d and e).

We have also examined the depth-integrated along-channel momentum balance for the Pamlico northern basin and found very different mechanisms. Fig. 3.10 shows the depth integrated momentums in the Pamlico northern basin. The balance is mainly maintained by the along-channel barotropic pressure gradient, surface wind stress and friction. Horizontal density gradient and earth rotation play very minor roles. Since

the Pamlico northern basin is aligned with the wind direction, the efficiency of surface stress is high enough to mix up the whole water column and push the water towards Oregon Inlet until steady state is achieved. In the shallow areas immediately inside the Outer Bank and along the west coast, wind overcomes the sea surface slope driving downwind currents. However, in the central region of the basin where water depth increases up to 7 meters, pressure gradient introduced by the sea surface slope overwhelms the wind stress. Upwind flow develops as shown in Fig. 3.7b. From the pattern of friction which changes sign from shallow regions to deep channel (Fig. 3.10d), we can also find the signature of this current pattern. We have also checked momentum balance on the northern section (figure not shown). Currents change sign along the section. But pressure gradient, towards the same direction, is relatively small in the shallow and increases gradually with depth. In Albemarle Sound, similar mechanism determines the circulation dynamics.

Vorticity analysis tells more. We show depth averaged equations of motion and continuity

$$\begin{aligned}
\frac{\partial u}{\partial t} &= -\frac{1}{\rho} \frac{\partial P}{\partial x} + \frac{1}{\rho} \frac{\tau_s^x - \tau_b^x}{H} + fv - N_x, \\
\frac{\partial v}{\partial t} &= -\frac{1}{\rho} \frac{\partial P}{\partial y} + \frac{1}{\rho} \frac{\tau_s^y - \tau_b^y}{H} - fu - N_y, \\
\frac{\partial \eta}{\partial t} + \frac{\partial(Hu)}{\partial x} + \frac{\partial(Hv)}{\partial y} &= 0.
\end{aligned} \tag{3.7}$$

where N_x and N_y are two nonlinear advection term. The continuity equation is

used to substitute the term $(\frac{\partial u}{\partial x} + \frac{\partial v}{\partial y})$. Then we will get the vorticity equation

$$\begin{aligned}
\frac{\partial \zeta}{\partial t} = & - \underbrace{\frac{1}{\rho^2} \nabla P \times \nabla \rho}_{\text{baroclinity}} + \underbrace{\frac{f}{H} \frac{\partial \eta}{\partial t} + \frac{f}{H} (\vec{U} \cdot \nabla H)}_{\text{topographic beta effect}} \\
& + \underbrace{\left\{ \frac{\partial}{\partial x} \left(\frac{\tau_s^y}{\rho H} \right) - \frac{\partial}{\partial y} \left(\frac{\tau_s^x}{\rho H} \right) \right\}}_{\text{wind stress curl}} \\
& - \underbrace{\left\{ \frac{\partial}{\partial x} \left(\frac{\tau_b^y}{\rho H} \right) - \frac{\partial}{\partial y} \left(\frac{\tau_b^x}{\rho H} \right) \right\}}_{\text{bottom stress curl}} \\
& + \underbrace{V_N}_{\text{non-linear term}} . \tag{3.8}
\end{aligned}$$

Vorticity in Fig. 3.11a and b demonstrates the flow pattern in the Pamlico northern basin very well. Under northeastward wind, positive vorticity occupies the eastern part of the northern basin while negative in the western part, indicating a Csanady type circulation. A reversed pattern shows under southwestward wind. Under both winds, the two main terms in vorticity equation are the surface wind stress curl and the bottom stress curl, which is consistent with the momentum analysis as shown in Fig. 3.12. From the sign in Fig. 3.12, we find wind stress curl is the driving factor while the bottom stress curl performs as resistance. Understandably, baroclinity is important in the southern basin but negligible in the northern basin and Albemarle Sound, since large buoyancy input exist in the southern basin while strong mixing in the northern basin and Albemarle Sound.

3.3. Seasonal evolution of circulation

At seasonal and shorter time scales, winds are a major force driving the currents in APS since astronomical tides are negligible. As shown in Fig. 2.1e, southeastward winds dominate during the winter whereas winds are prevailing northeastward during

the summer. Winds are variable and relatively weaker during the spring and fall transition periods. Now we investigate how currents in APS are influenced by seasonal shifts in the prevailing wind patterns. Are the seasonal mean currents mainly driven by prevailing winds or horizontal density gradient? How can the idealized cases in the previous section be applied to the explanation of circulation under the realistic wind forcing? Figures 3.13-16 show the surface and bottom distributions of seasonal-mean currents: winter (Dec.-Feb.), spring (Mar.-May), summer (Jun.-Aug.), and fall (Sep.-Nov.). For easy comparison, we also plot the frequency distribution of wind directions and seasonal-mean sea level distribution.

In the spring, wind directions shift and baroclinic effects are strongest. The spring circulation pattern is similar to the annual mean circulation pattern, with the surface water leaving Albemarle Sound, Neuse and Pamlico Rivers, and the bottom water leaving the Ocracoke and Hatteras Inlet (Figs. 3.13c and d). The total flows from the four rivers reached a high mean value of $2000 \text{ m}^3\text{s}^{-1}$ during the spring of 2003. Sea level during the spring also shows a similar spatial distribution as the annual mean, although high river flows lead to even higher sea levels in Albermarle Sound, Neuse and Pamlico Rivers (Fig. 3.13b). Winds were highly variable during the spring transition period, although northeastward and southwestward winds were more frequent and stronger than winds in other directions (Fig. 3.13a). The seasonal mean wind speed was weak. Thus the spring circulation is primarily driven by strong horizontal density gradients between the rivers and inlets. Compared with wind, large amount buoyancy input generates much stronger density-driven flow.

The northeastward winds were exceptionally strong during the summer of 2003 (Figs. 2.1e and 3.14a). They drive strong eastward surface outflows from Pamlico and Neuse Rivers while a westward flow return into Neuse and Pamlico River at the bottom. Strong two-layer flow develops because of the wind straining effect generated by the eastward components of summer winds. Water level is higher on the northern end of Pamlico Sound (Fig. 3.14b). In the shallow region of the Pamlico northern basin, very strong currents follow the wind direction at both surface and bottom. The northeastward winds also drive eastward flows in Albemarle Sound, leading to high sea levels at its eastern side and forcing a strong southward flow through the narrow Croatan and Roanoke Sounds. This southward current merges with the northward current along the Outer Banks before exiting to the Atlantic Ocean through Oregon Inlet. However, we see a southwestward flow in the deep region of the Pamlico northern basin which opposes the wind direction (Fig. 3.14d). These flows are mainly driven by the north-south sea level slope in Pamlico Sound that is set up by the northeastward winds (Fig. 3.14b), revealing a laterally sheared response to the wind forcing, which is the same as the Csanady type currents under idealized northeastward wind. Comparing the summer case and the idealized northeastward wind case (Fig. 3.5 and 3.14), we see high similarity. To the lowest order, the summer mean circulation in APS is controlled by the prevailing northeastward wind. Of course, due to the differences of mixing strength, some details, like the current strength in the middle part of the northern basin, are not exactly the same between the summer mean circulation and that in the idealized case. We also notice that on the

shallow side along the Outer Bank, the wind stress is so strong so that it forces a northeastward flow at all depths. It is interesting to note that the northward current on the inner shelf outside the Outer Banks is strongest during the summer as the Gulf Stream shifts northward and intrudes into North Carolina Coasts.

Winds were variable and relatively weak during the fall transition (Fig. 3.15a). The southwestward and northeastward winds were more frequent, but southwestward winds slightly dominated, resulting in a seasonal mean wind pointing to the southwestward direction. This caused sea-level pile up at the southwestern part of Pamlico Sound, but the sea-level slope is only half of that reached during the summer (Fig. 3.15b). The surface current pattern looks similar to the spring pattern, although the prevailing southwestward winds generate southwestward current in the shallow eastern part of Pamlico Sound (Fig. 3.15c). The bottom current also looks similar to the spring pattern, although the northward current in Pamlico Sound is stronger and is probably driven by the sea-level slope (Fig. 3.15d).

The prevailing wind direction during the winter was southeastward (Fig. 3.16a). This southward wind drives strong surface outflows from Albemarle Sound, Pamlico and Neuse Rivers (Fig. 3.16c). The bottom currents generally move in the opposite direction to the surface currents (Fig. 3.16d) in the southern basin, since the eastward components of winds push sea levels higher on the Outer Banks (Fig. 3.16b), which together with the east-west density gradient drives the counter current at the bottom. Water from Albemarle Sound moves southward along the Outer Banks while two

flow branches originated from Pamlico and Neuse Rivers cross the Pamlico Sound towards the Outer Banks. In the Pamlico northern basin and Albemarle Sound, the southeastward winds driven more lateral-sheared circulations with downwind flow in the shallow and upwind in the deep, which is very similar to the pattern under idealized southeastward wind (Fig. 3.6c and d).

In summary, we have employed ROMS to develop a new 3D hydrodynamic model for APS and used it to investigate the circulation dynamics in this lagoonal estuary. Although the vertical stratification is weak, the geographic separation between the rivers and inlets generates large horizontal density gradients. Because of their layouts, the flow responses of three separated regions to the same wind are very different, depending on the relative importance of wind stress compared with horizontal salinity gradient. Using idealized wind stress, we introduced Wedderburn number and Csanady linear solution to explain the wind's effects. Using year 2003 as an example, we conducted hindcast simulations. The seasonal circulation is driven by seasonally shifting prevailing winds but is also affected by the horizontal density gradients. The typical current response to the wind forcing in the shallow APS is a horizontally segregated flow as the winds generate the sea-level slope and pressure gradient which work against the wind stress. In the Pamlico southern basin where horizontal salinity gradient is large, the baroclinic effect and wind straining effect have to be considered.

Both flow pattern and momentum balance show very good agreement between the idealized cases and realistic simulation in two seasons (summer and winter), which confirms that the seasonal circulation is primarily driven by seasonally shifting prevailing winds. However, although basic patterns from idealized wind cases and realistic cases are similar, they differ in details. One reason is the different levels of mixing which will yield different eddy viscosities and sequentially different Ekman depth. Valle-Levinson (2007) discussed the estuarine exchange flow in terms of the Kelvin and Ekman numbers. When Ekman number is big enough (larger than 1), lateral exchange circulation will not show up no matter how wide the basin is. Idealized winds can reproduce the basic wind-driven circulation pattern but cannot represent the strength of mixing induced by realistic winds.

One direct example is the comparison between no wind case and the spring of 2003. In the Pamlico southern basin, we saw lateral circulation with inflow to the north while outflow to the south under no wind condition (Fig. 3.11b). However, in the spring of 2003, although the mean wind is very weak (very close to zero), the transitional wind produced high level of mixing deriving a deep Ekman depth. Under this big Ekman number (>0.5), we cannot see the lateral circulation during the no wind condition. Instead, a vertical two-layer circulation exists (Fig. 3.13c and d). The seasonal wind is the primarily driving force for the seasonal circulation. But wind induced mixing modulates the details of this circulation pattern.

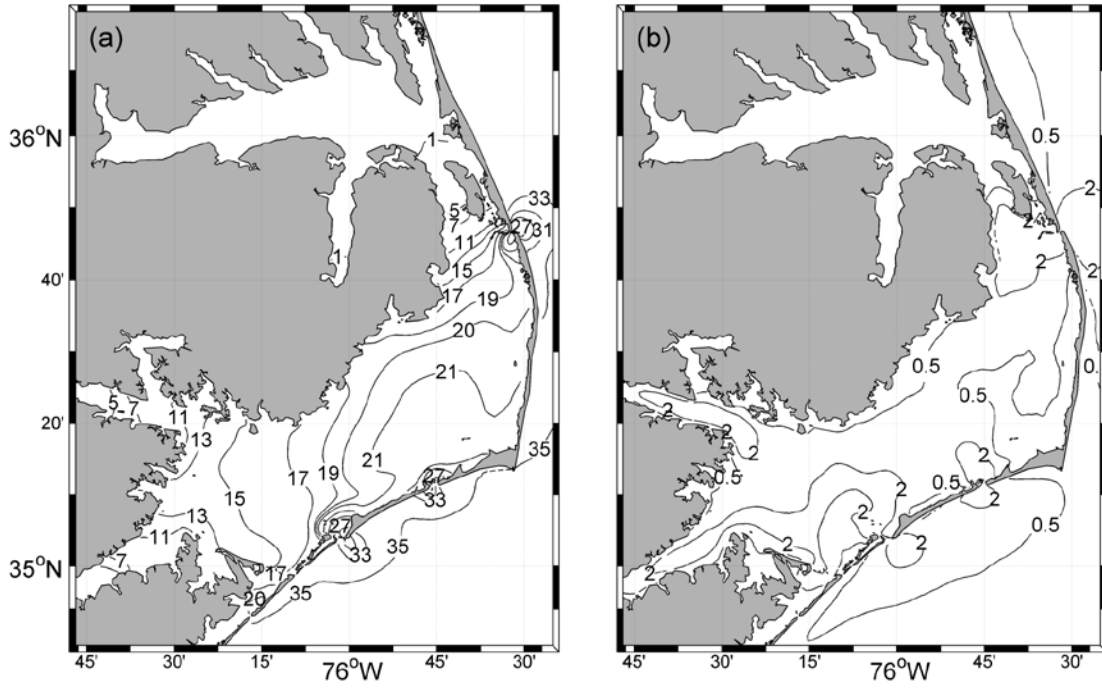


Figure 3.1 Mean salinity (in psu) distribution at the surface of APS. (b) Distribution of mean bottom-to-top salinity difference.

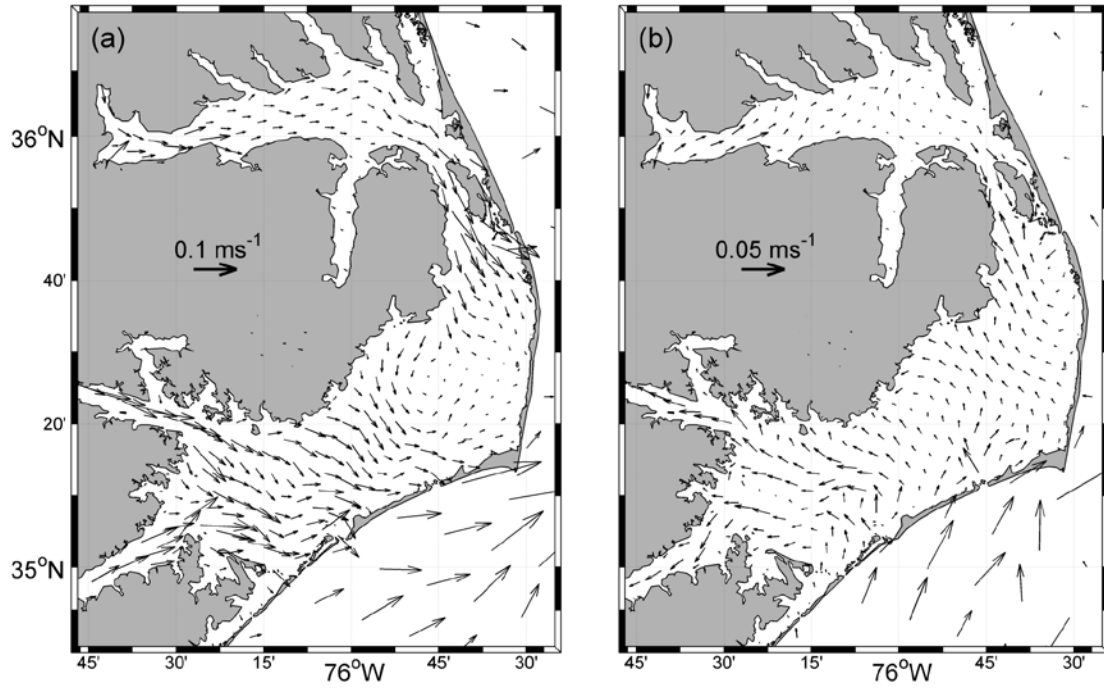


Figure 3.2 Mean circulation patterns at the (a) surface and (b) bottom of APS.

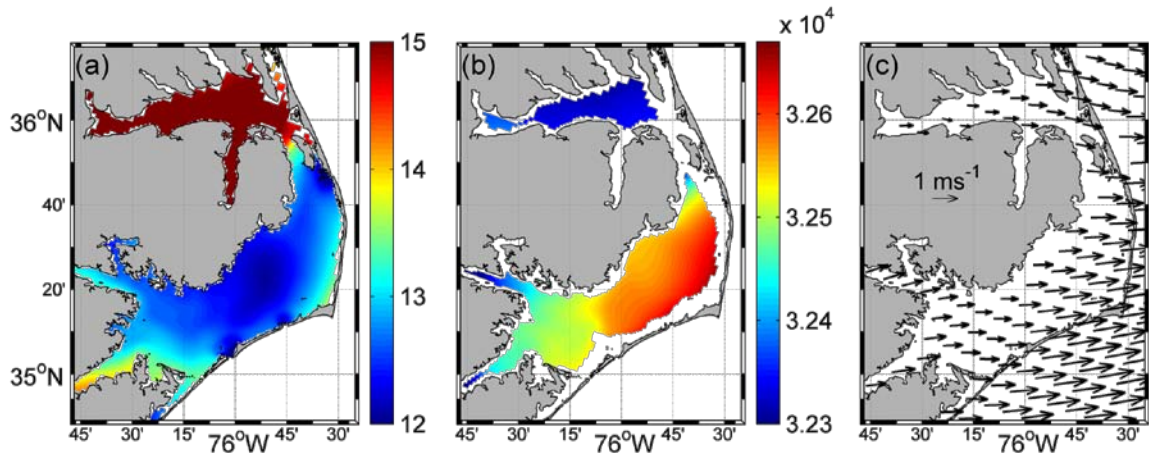


Figure 3.3 Distributions of (a) mean sea level (cm), (b) hydrostatic pressure (Pa) at 3-m depth, and (c) mean wind speed vectors (ms^{-1}) over APS.

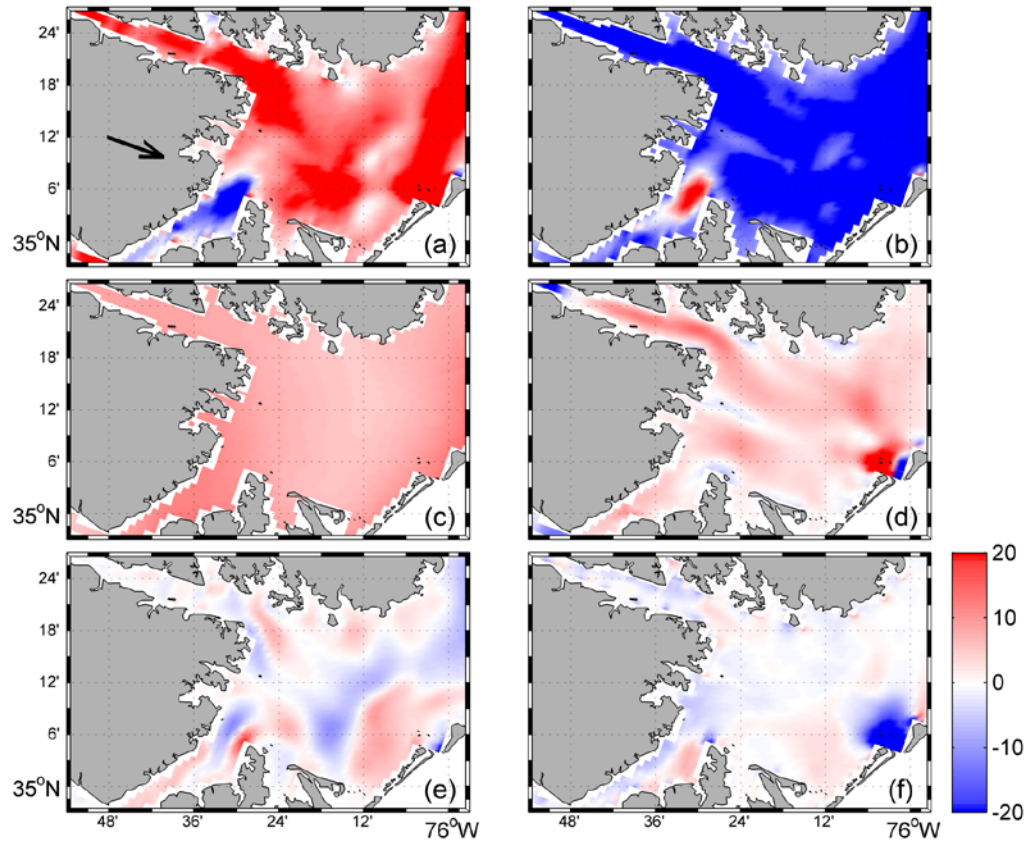


Figure 3.4 Distributions of depth-integrated (a) barotropic and (b) pressure gradient, (c) surface stress, (d) bottom stress, depth-integrated (e) Coriolis force and (f) nonlinear advection in the southern Pamlico Sound, all in the direction indicated by the arrow in (a). They are in the unit of m^2s^{-2} and multiplied by 10^{-6} .

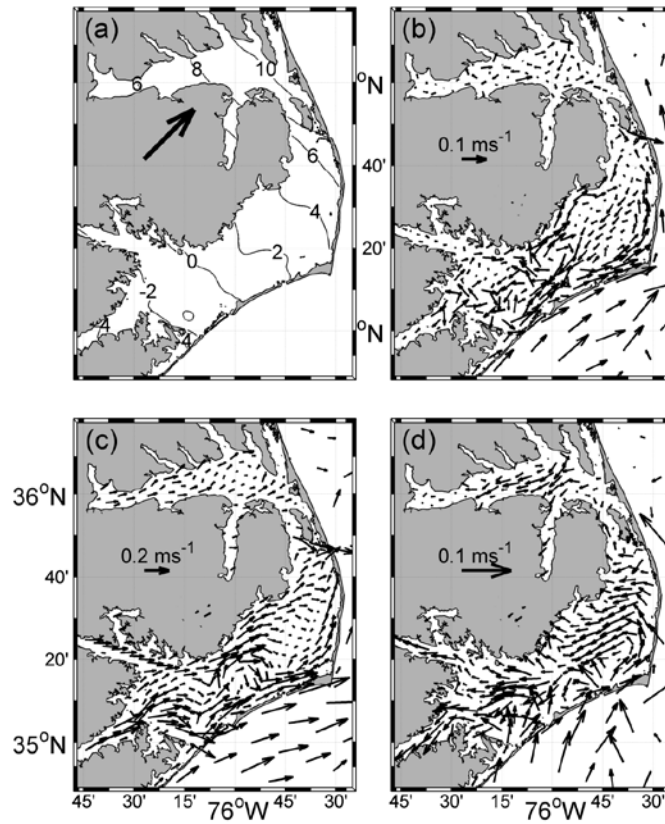


Figure 3.5 Mean circulation pattern under constant northeastward wind. Distributions of seasonal mean (a) sea level, (b), depth averaged (c) surface and (d) bottom currents.

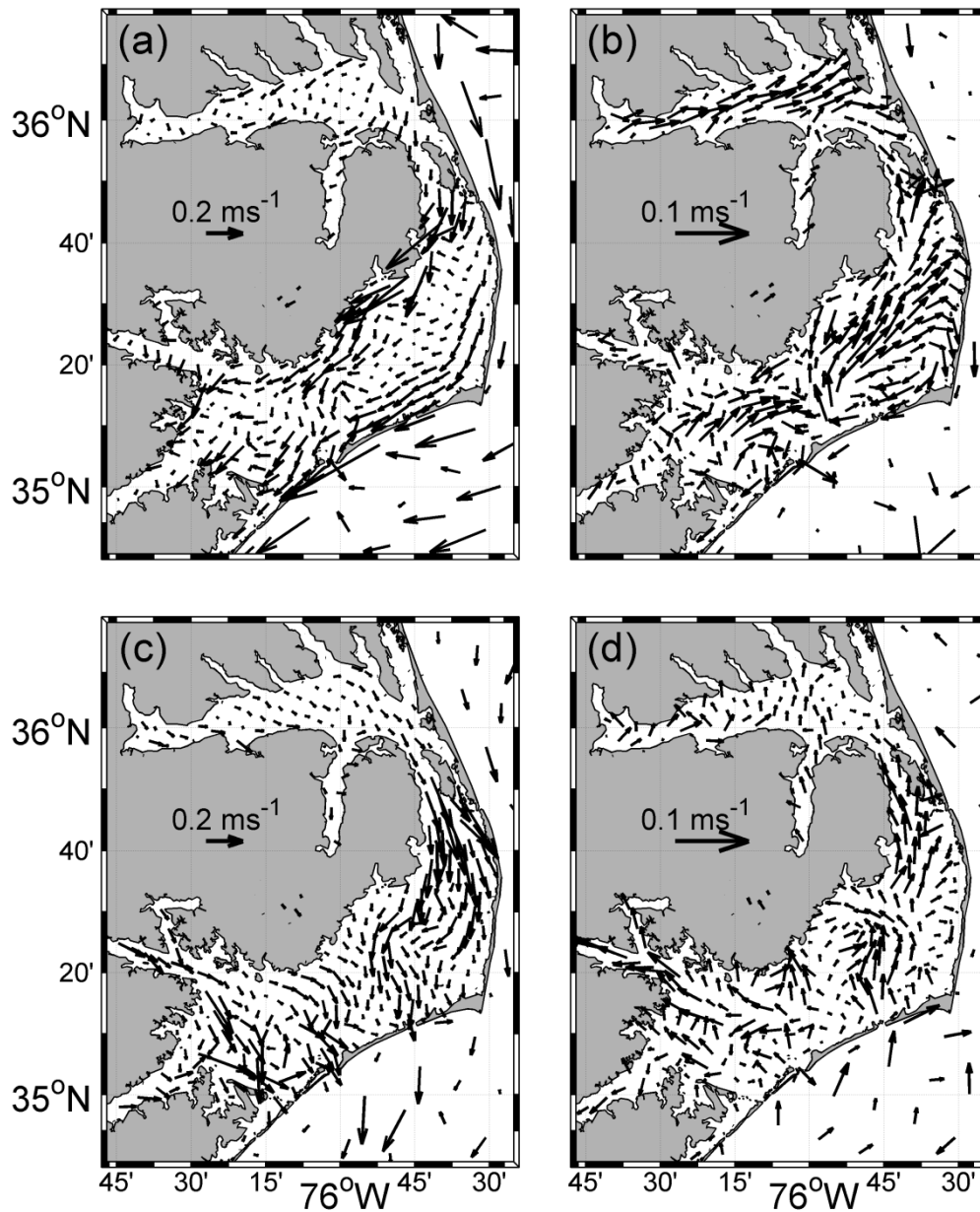


Figure 3.6 (a) surface and (b) bottom currents under constant southwestward wind; (c) surface and (d) bottom currents under constant southeastward wind.

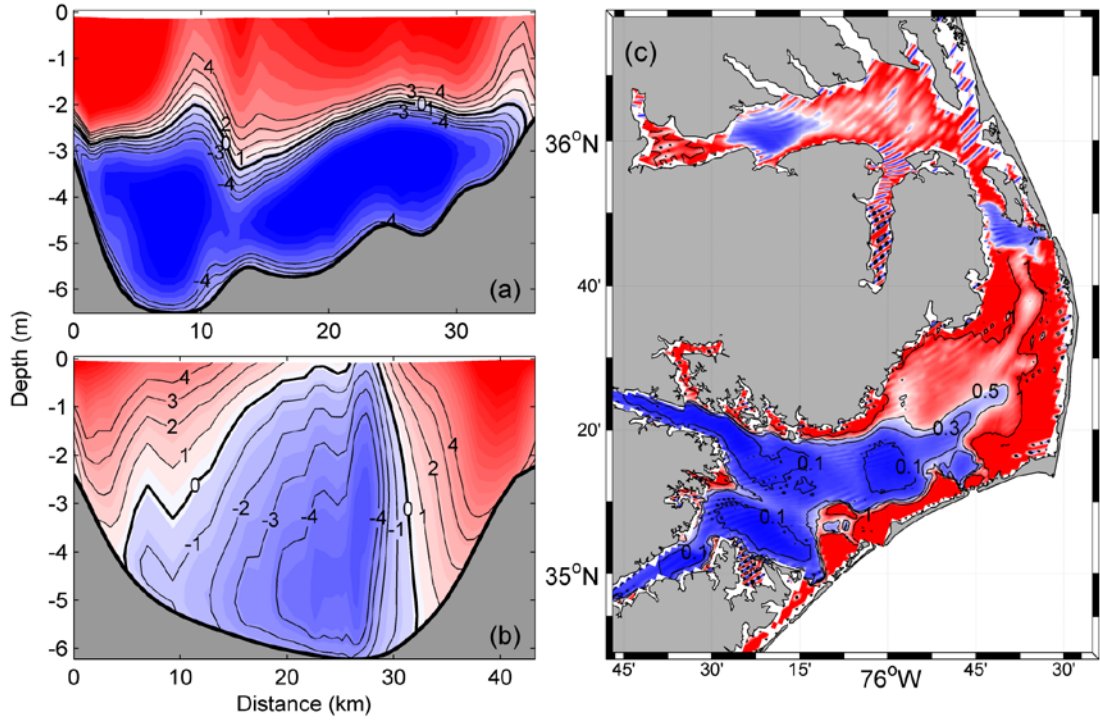


Figure 3.7 Distributions of cross-section [S1 and N1 in Fig.1.1a] (a) and (b) currents (in 10^{-2} ms^{-1}), (c) Distribution of Ekman number in northeastward wind case.

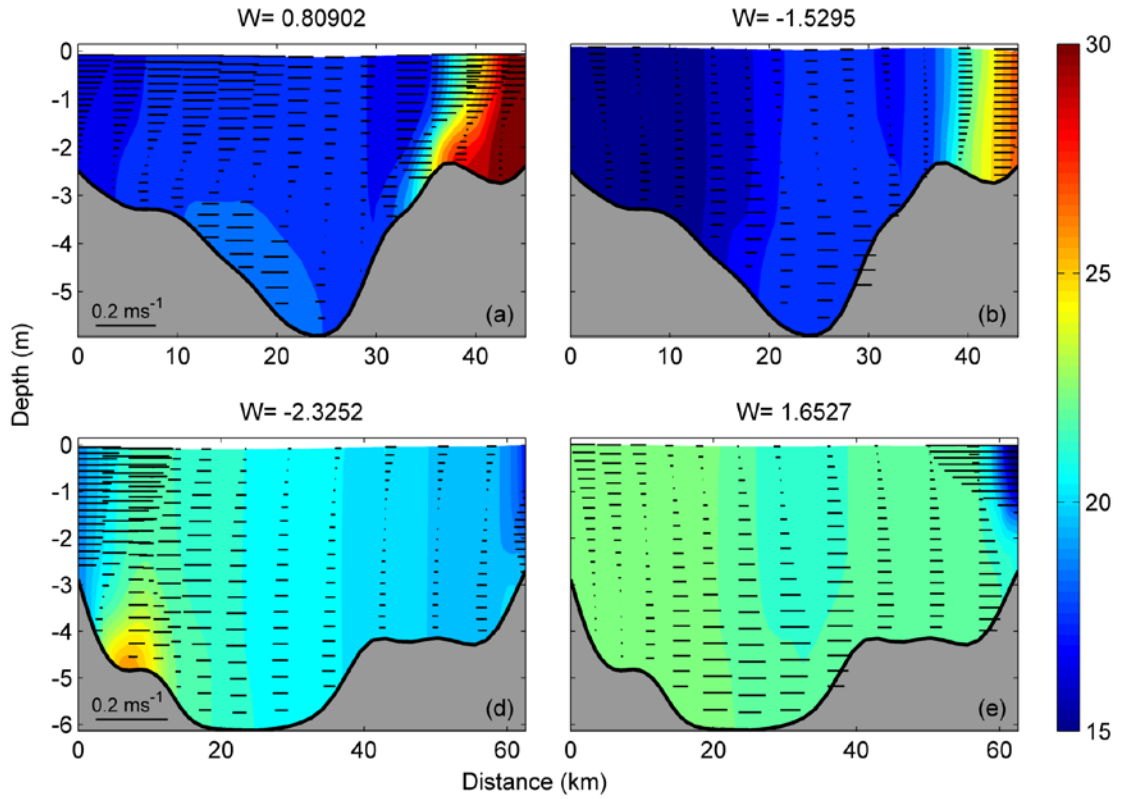


Figure 3.8 Wind straining vs wind mixing effect. Distributions of currents and salinity on the two along-channel sections [S2 and N2 in Fig.1.1a] (a) and (d) during northeastward wind events, (b) and (e) during southwestward wind events, and the corresponding Wedderburn numbers.

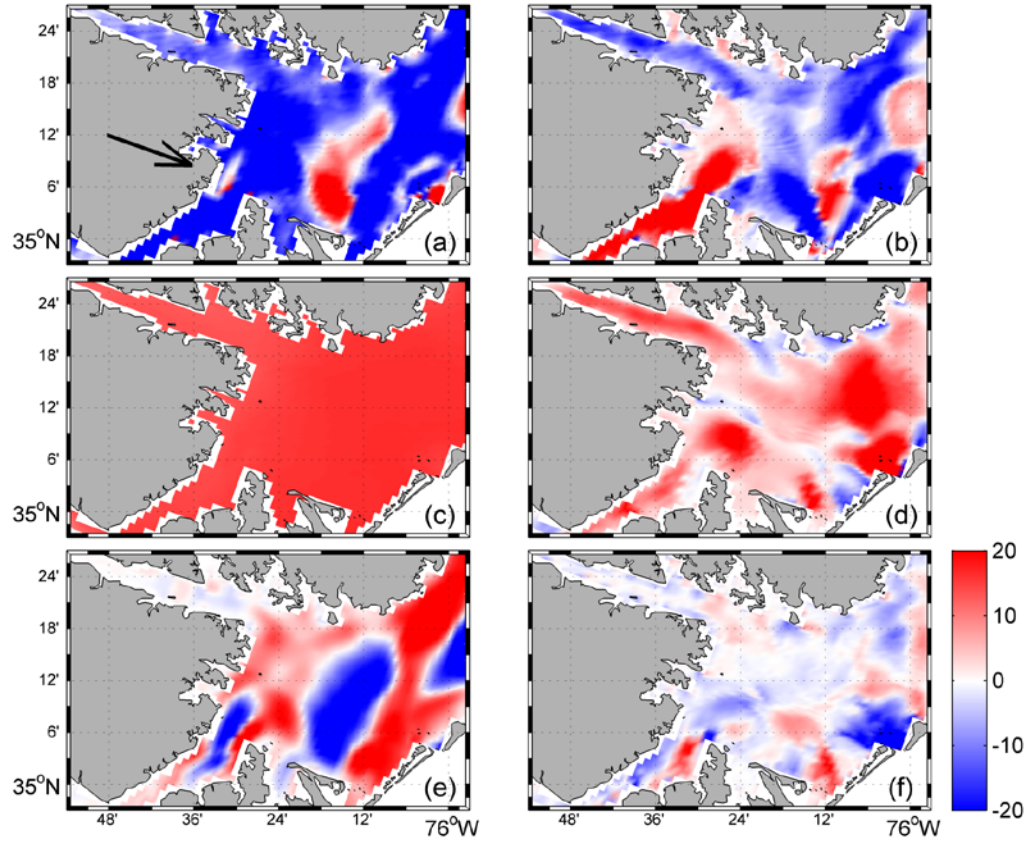


Figure 3.9 Distributions of depth-integrated (a) barotropic and (b) baroclinic pressure gradient, (c) surface stress, (d) bottom stress, (e) Coriolis force and (f) nonlinear advection in the southern Pamlico Sound under northeastward wind, all in the direction indicated by the arrow in (a). They are in the unit of m^2s^{-2} and multiplied by 10^{-6} .

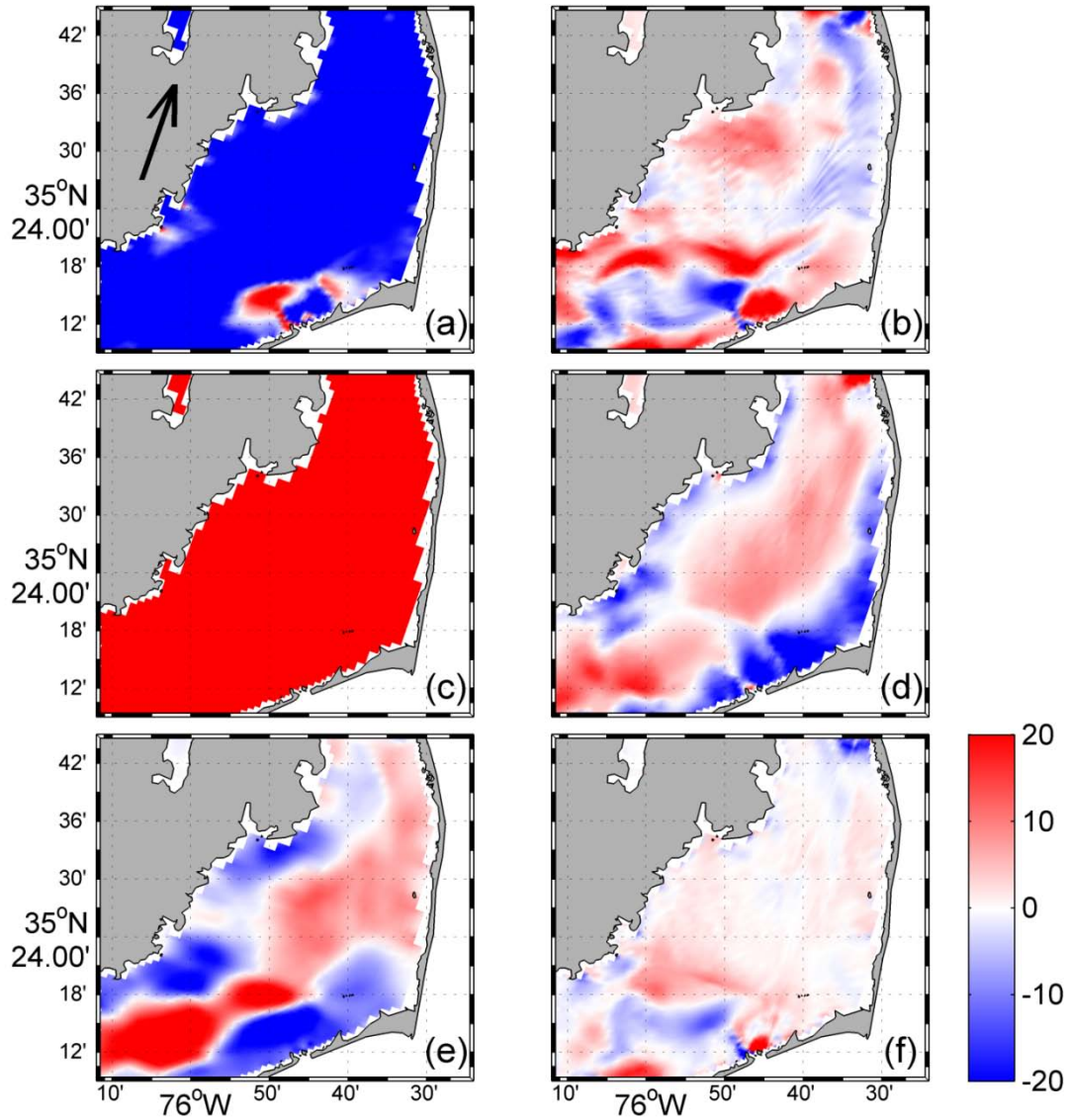


Figure 3.10 Distributions of depth-integrated (a) barotropic and (b) baroclinic pressure gradient, (c) surface stress, (d) bottom stress, (e) Coriolis force and (f) nonlinear advection in the northern Pamlico Sound under northeastward wind, all in the direction indicated by the arrow in (a). They are in the unit of m^2s^{-2} and multiplied by 10^{-6} .

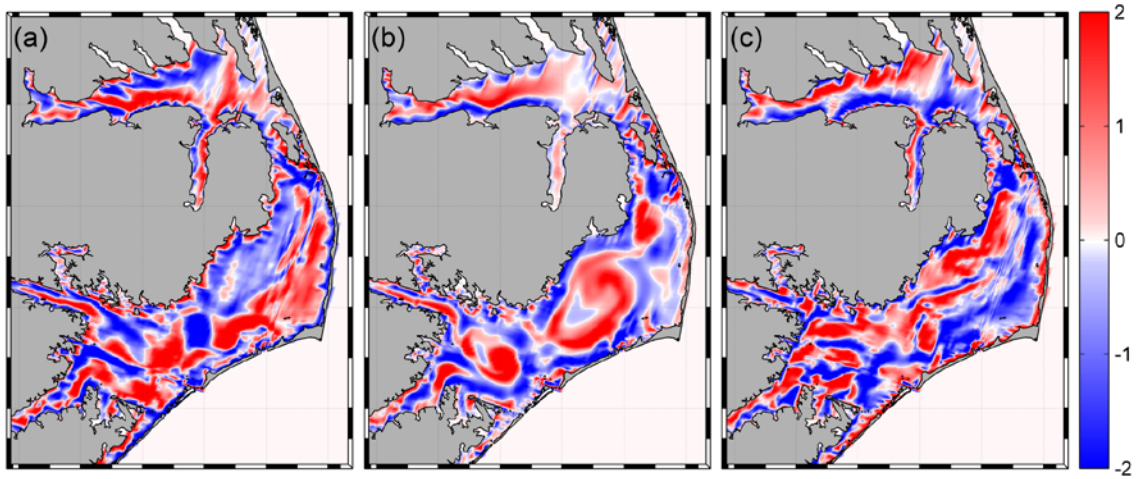


Figure 3.11 Distributions of vorticity in 10^{-5} s^{-1} (a) during northeastward wind events, (b) without wind, (c) during southeastward wind events.

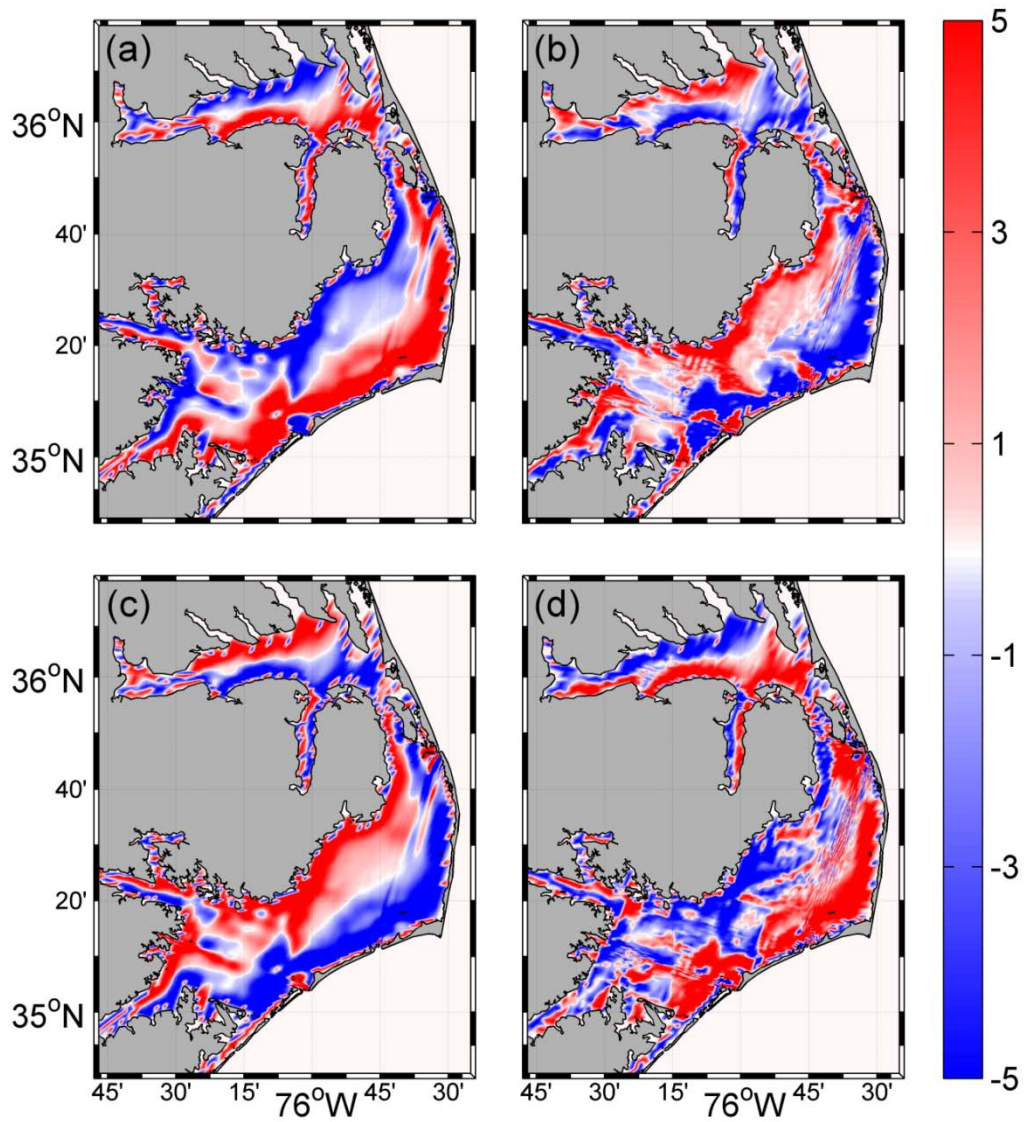


Figure 3.12 Distributions of PV balance terms in 10^{-10} s^{-2} under northeastward and southeastward wind conditions: (a) and (c) wind stress curl, (b) and (d) bottom stress curl.

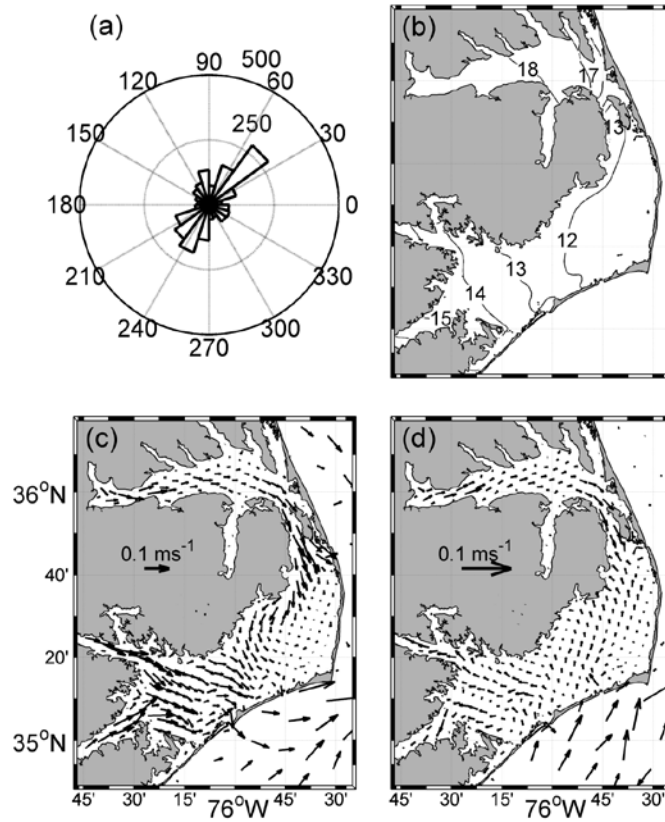


Figure 3.13 Mean circulation pattern during spring. (a) Frequency distributions of wind directions. Distributions of seasonal mean (b) sea level, (c) surface and (d) bottom currents.

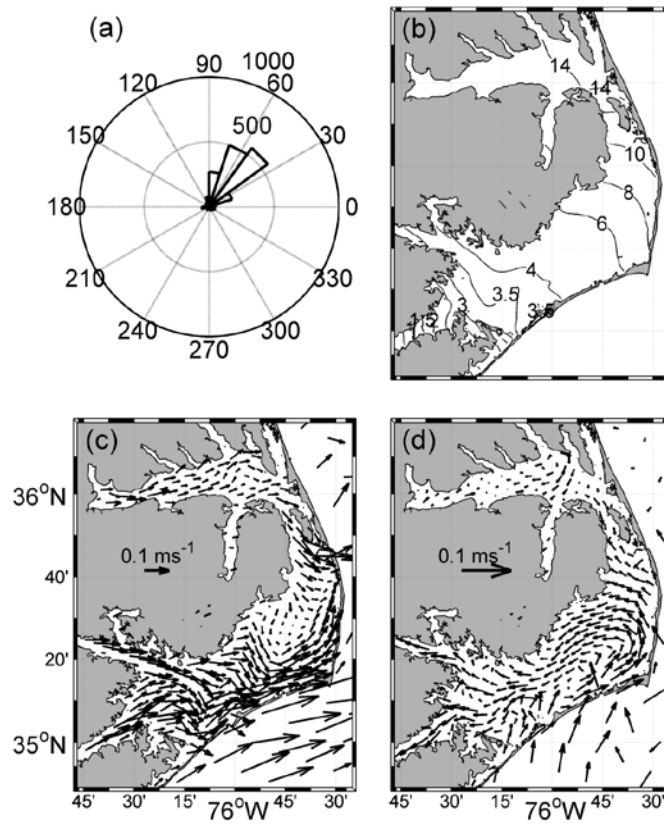


Figure 3.14 Mean circulation pattern during summer. (a) Frequency distributions of wind directions. Distributions of seasonal mean (b) sea level, (c) surface and (d) bottom currents.

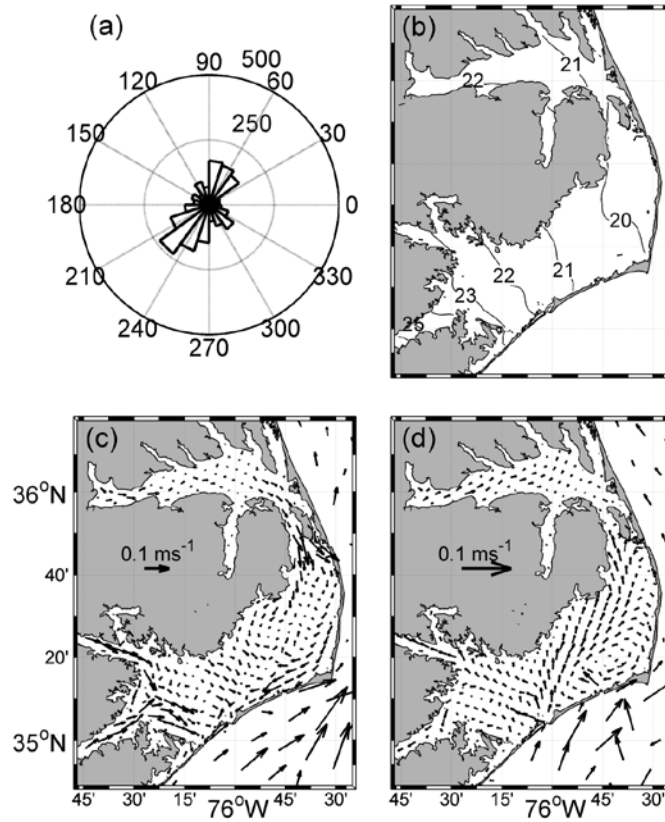


Figure 3.15 Mean circulation pattern during fall. (a) Frequency distributions of wind directions. Distributions of seasonal mean (b) sea level, (c) surface and (d) bottom currents.

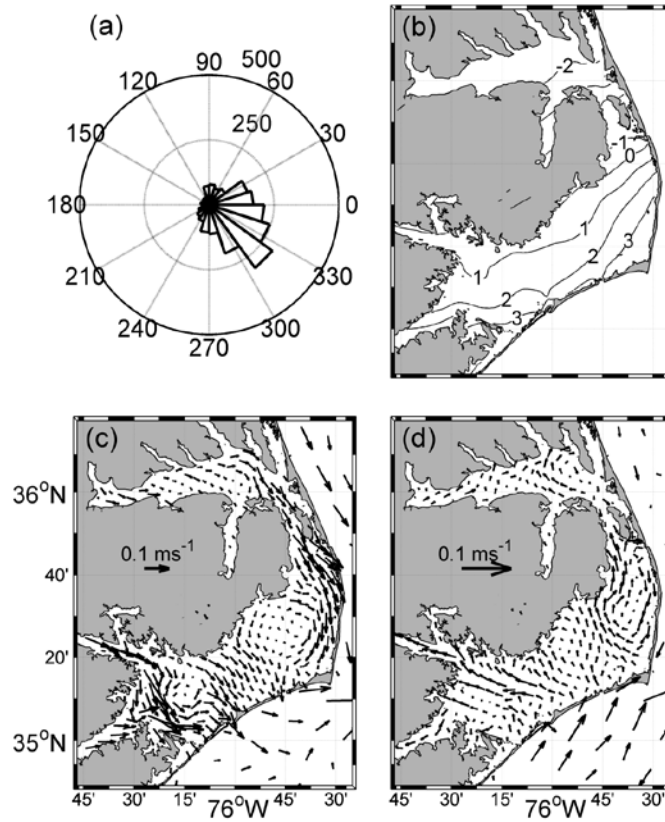


Figure 3.16 Mean circulation pattern during winter. (a) Frequency distributions of wind directions. Distributions of seasonal mean (b) sea level, (c) surface and (d) bottom currents.

Chapter 4: Wind's effect on stratification

APS receives freshwater from four rivers and exchanges salt with the Atlantic Ocean through the three inlets. The river discharges have a well-defined seasonal cycle: high flows during spring and low flows during summer. Stratification, which is the key to vertical momentum exchange processes, has been widely investigated in other estuary systems like Hudson River, York River and Chesapeake Bay. How do the river flows and rainfall affect the seasonal evolution of the stratification in APS? How does the wind affect stratification in this wide, shallow and highly frictional estuary? In this chapter effects of wind and strong rainfall events on stratification will be studied.

4.1. Wind straining and mixing effects

Wind's effect on stratification is achieved by the competition between wind straining and direct wind mixing. Hereafter, the effect of axial wind will be mainly focused on. Since the vertical salinity difference is so low, the stratification in Albemarle Sound will not be studied.

In the Pamlico southern basin, during moderate down-estuary wind, the horizontal salinity gradient is strained. Fresh water penetrates farther downstream towards Ocracoke Inlet at the surface while saline water intrudes farther landward at the bottom. Direct wind mixing is relatively weak compared with the straining effect, so the stratification is intensified. On the other hand, during moderate up-estuary

wind event, the isopycnal is tilted up as the fresh water at the surface is constricted at the river mouths and the saline water intrudes less at the bottom. Stratification is greatly reduced. As the wind speed increases and the mixing become strong enough, the water column becomes vertically homogenous (Fig. 3.10c). Stratification eventually disappears. A laterally segregated current which is consistent with Csanady's analytical solution for wind-driven flow over laterally varying bathymetry develops, indicating that wind-driven axial flow dominates over gravitational circulation [$W > 1$].

4.2. Semi-durnal Seiching

Luettich et al. (2002) found that over half of the along channel velocity variance associates with roughly the semi-diurnal frequency band. Velocity in this frequency range is episodic, has a typical magnitude of 10 cm s^{-1} and often reaches twice this speed. By using wavelet analysis which is a highly effective technique for discriminating times, they found the semi-diurnal motion was strong and identified a predominant 13.2-h period in the along channel component of both 10-week wintertime and 10-week summertime current meter records. The semi-diurnal signal was also captured by a barotropic model simulation using idealized wind forcing.

Since the astronomical tide in APS is negligible, owing to the APS's virtual isolation from the coastal ocean by the North Carolina Outer Banks barrier island chain, the episodic nature of the velocity signal suggests that the semi-diurnal signal is generated within the APS, presumably due to meteorological forcing.

Hutchinson (1957) summarized that a half-wavelength seiche had been observed frequently in lakes. The propagation of such a seiche in shallow water is governed by

$$\frac{2L}{T} = \sqrt{gh} \quad (4.1)$$

where L is the basin length, T is the oscillation period, g is the acceleration of gravity and h is the water depth. This kind of seiche also exists in APS. However, due to the irregular geometry and bathymetry of the APS, appropriate values of the basin length and the water depth are not immediately clear. From the idealized model simulation, Luettich et al. (2002) confirmed that semi-diurnal signal was introduced by the resonance to oscillatory wind and indentified an average “seiche depth” of 3.5m and a “seiche length” of 139 km. This length is close to that of the long axis of Pamlico Sound, although the depth is approximately 25 percent less than the sound’s 4.5m mean bathymetric depth.

Given the absence of a tidal current, this motion plays a significant role in determining the position and strength of the salt wedge, the thickness of the diffusive bottom boundary layer and the overall dispersion characteristics of the system especially in the Pamlico southern basin. This semi-diurnal seiche generates strong mixing which reduces the total stratification level in APS. We applied 13.2-h and 48-h rotating winds of the same speed (5 m s^{-1}). The 13.2-h wind excites a resonance of APS while no seiche responds to the 48-h wind. In Fig. 4.1, the N^2 during 13.2-h wind is significantly smaller than that during 48-h wind indicating stronger mixing when the seiching is excited. Rotating wind with prevailing eastward or westward direction is more efficient to mix the water column. One reason is that the fetch is

longer in east-west direction. The seiche can even be found 5 days after the wind stops. And N^2 is also significantly smaller after 13-h wind event.

Bottom friction plays an important role in generating mixing and dissipating the seiching energy. In order to study the nature of mechanics, we conducted two numerical experiments under 13-h winds: one with high bottom stress coefficient (bottom roughness height of 1mm), the other with very low one (0.01mm). We find the thickness of the diffusive bottom boundary layer is the key to the overall dispersion and stratification characteristics of the system. With high bottom stress coefficient, a thicker bottom boundary layer generated by the seiche merges with the surface mix layer, reducing the stratification even farther during wind events. Short time (less than 5 days) after the idealized wind, the bottom boundary layer still exists. Because of the existence of this bottom boundary layer, stratification is noticeably lower under high bottom stress.

4.3. Effects of fresh water input on stratification

Although freshwater inflows from the rivers and salt exchanges across the inlets are the two dominant terms affecting salinity in APS, it has been suggested that local precipitation and evaporation over APS may influence salinity in APS (Roelofs and Bumpus, 1953; Pietrafesa, 1983). Although the evaporation and precipitation are nearly in balance over a year, precipitation exceeds evaporation during spring and winter whereas the reverse is true during the summer. To investigate the effects of local precipitation and evaporation, we plot the time series of the total river discharge Q and compare it again the time series of the precipitation minus evaporation (P-E)

integrated over the surface area of APS (Figs. 4.2b and c). Understandably, P-E time series shows higher frequency temporal fluctuations than Q. Nevertheless, short peaks in P-E reach as high as 50% of the peaks in Q. During early spring precipitation causes a small increase of APS volume whereas evaporation causes a decrease in the volume during the summer and early fall. By the beginning of October of 2003, the total evaporation exceeds the total precipitation by $1.6 \times 10^9 \text{ m}^3$ (about 50% of the total volume variation), which persists until the year end even though $P \approx E$ in the final 3 months. Hence, the local evaporation and precipitation play very important role in changing the volume and sequentially the salinity and stratification in APS.

Climatic perturbations by drought-flood cycles, tropical storms, and hurricanes are increasingly important in Mid-Atlantic estuaries, leading to ecosystem-scale responses of the plankton system with significant trophic implications. Six major hurricanes, magnitude 2 or greater on the Safford–Simpson scale, have made landfall in North Carolina between 1996 and 1999. Hurricanes Dennis (September 4–5) and Floyd (September 16), which passed through North Carolina during a 12-day period in September 1999, and Hurricane Irene, which passed near the North Carolina coast on October 17, 1999 inundated the region with unprecedented rainfall (up to 1 m), causing prolonged record flooding (50- to 500-year flooding) in the watershed of APS. Floodwaters from the three sequential hurricanes inundated coastal rivers and impacted the hydrologic.

The central part of the Pamlico River basin received 96 cm of rain during September and October, 1999, or about 85% of the average annual rainfall. Freshwater inflow to PS during September and October 1999 was equivalent to about 83% of the total volume of the Sound. Typically, mean inflow volume for these two months is 13% of the Sound volume. The amount of fresh water input in short time greatly freshened the whole system. One monitoring station in western Pamlico Sound observed a drop of 19 psu of surface salinity and 15 psu of bottom salinity after the event.

Simulation of year 1999 is started from the end of year 1998 simulation. Fig. 4.3a and b shows the daily river discharge in 1999. Late September and early October show unprecedented high fresh water amount compared with the rest time of the year. Wind condition is similar as that in 2003 with transitional winds in the spring and fall, prevailing northeastward wind in the summer, and southeastward wind in the winter.

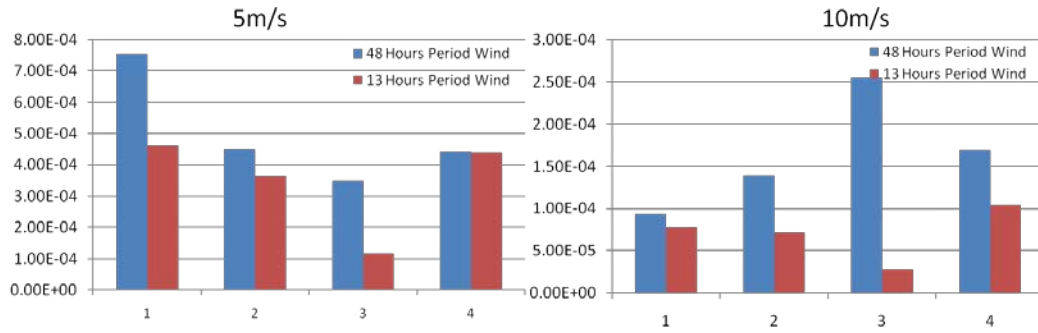
The model simulation is validated against the observations in Paerl et al. (2001). A comparison of pre- and post-hurricane salinity regimes throughout these estuaries can be found from the Neuse River Modeling and Monitoring (ModMon) program data. Historic late summer salinities are typically at their maximum of 10–13 psu near the mouths of Pamlico and Neuse Rivers, whereas surface salinities in southwestern Pamlico Sound also reach maximum values from 15 to 20 psu in September (19) (Fig. 4.4a). The week before Hurricane Floyd, surface salinities at stations in the western Pamlico Sound ranged from 18 to 20 psu. Two weeks after the passage of Hurricane

Floyd, surface salinity averaged 8.96 ± 1.4 psu, or less than half of typical values. Our model captures the post-hurricane freshening very well as shown in Fig. 4.4a.

As a result of this high amount of buoyancy input, the stratification at the monitoring station shown in Fig. 4.4b was dramatically increased. The averaged vertical salinity difference (bottom salinity minus surface salinity) is 1.5 psu two weeks before Hurricane Floyd. It increased up to 12.5 psu after the hurricane passage.

By comparing Fig. 4.5 and Fig. 4.6, we can find how the whole system responded to the freshwater input. Fig. 4.5a shows the mean surface salinity two weeks before the hurricane event. The 13-psu isohaline reaches as far as the mouths of Pamlico River and Neuse River. As mentioned in Chapter 3, the APS lacks vertical salinity difference. Fig. 4.5b shows the mean vertical difference which is mostly lower than 2. However, after the event, the 13-psu isohaline is pushed seaward reaching the middle of Pamlico Sound with strong stratification spread from the river mouth to almost the whole basin indicating by the 2-psu vertical salinity difference contour line in Fig. 4.6b.

In an estuary, exchange flow is always associated with stratification. Naturally, surface currents become strong due to high amount of fresh water input. As a result of the increased stratification and strengthened surface currents, the return flow at the bottom also increases, leading to a strong two-layer gravitational circulation in APS (Fig. 4.7a and b).



1=westerly wind; 2=southwesterly wind;
3=easterly wind; 4=northwesterly wind.

Figure 4.1 Basin-wide mean N^2 in Pamlico Sound under 5 and 10 ms^{-1} wind condition. 1 to 4 stand for four prevailing directions.

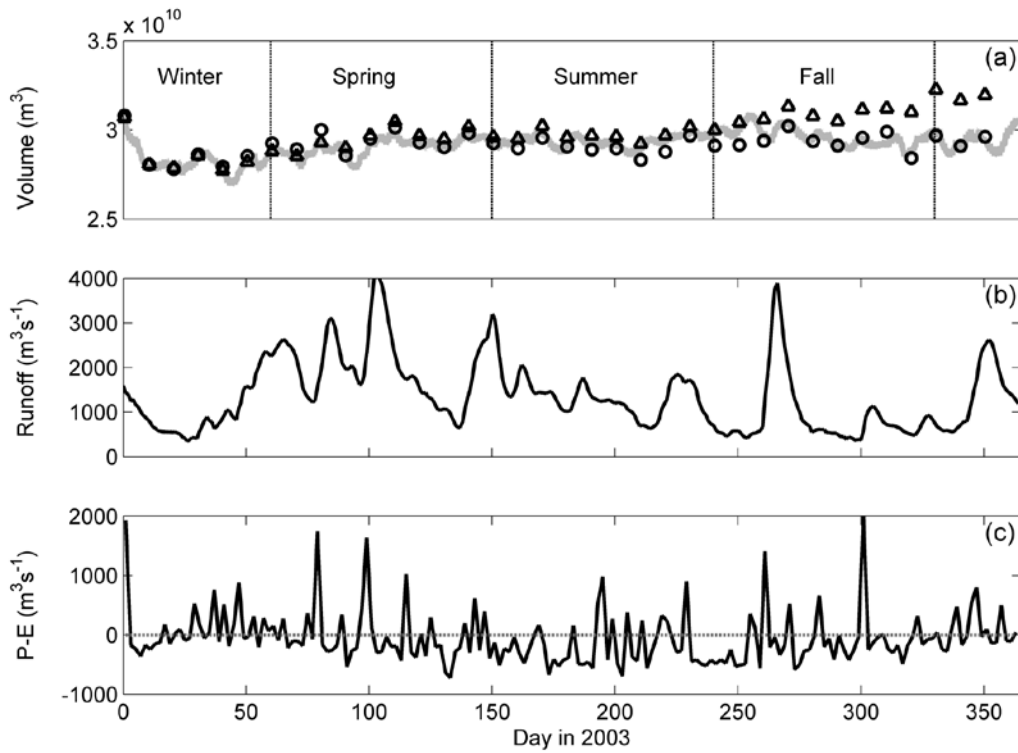


Figure 4.2 (a) Time series of total volume (grey) in APS, integrated volume flux (open circles) including river flows, precipitation minus evaporation (P-E) and transports through the inlets, and integrated volume flux (triangles) including river flows and inlet transports only. Time series of (b) total discharges from the four rivers and (c) net precipitation minus evaporation integrated over the surface of APS.

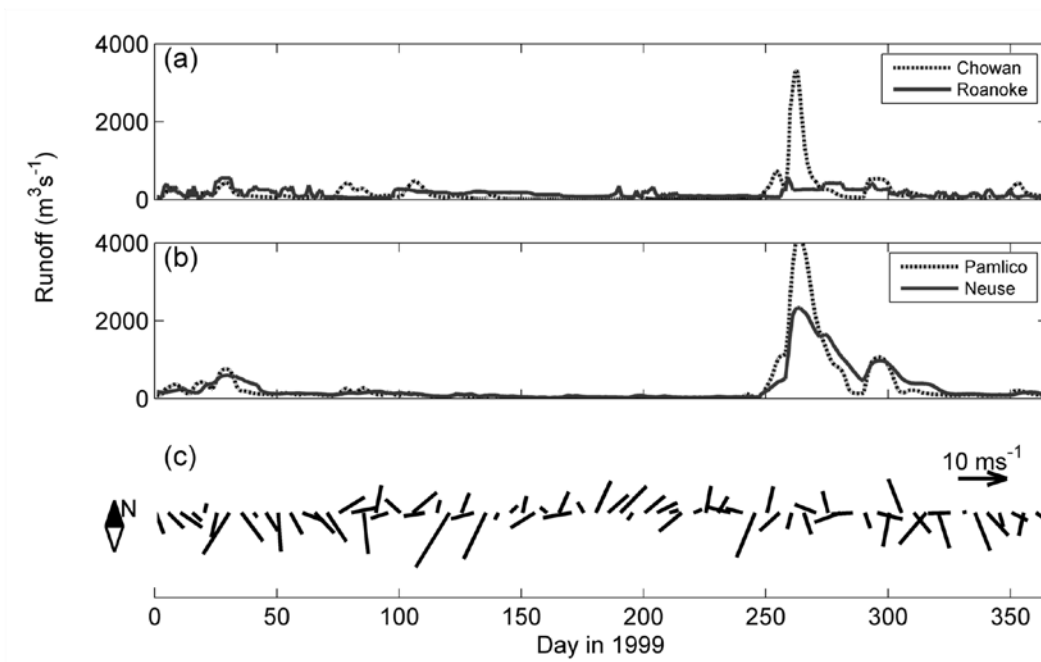


Figure 4.3 Discharges from (a) Chowan (dotted) and Roanoke (solid) Rivers, (b) Pamlico (dotted) and Neuse (solid) Rivers in 1999. (c) Weekly mean wind speed vector at a central location in APS.

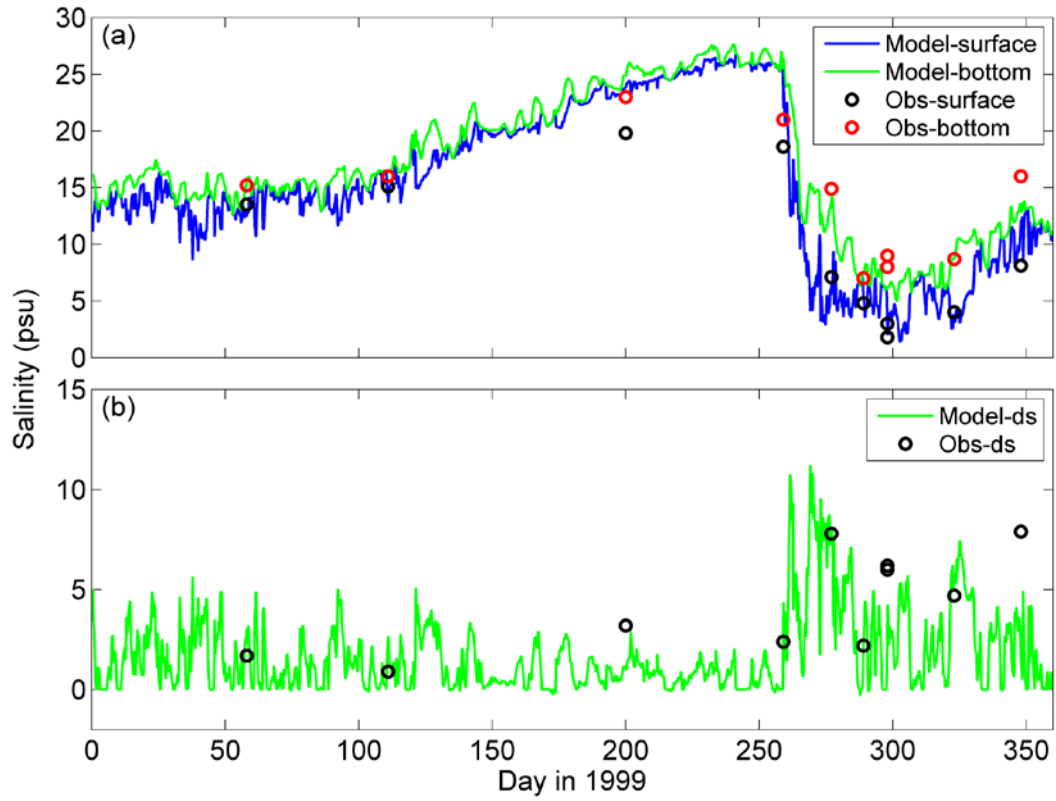


Figure 4.4 (a) Comparisons of both surface and bottom salinity, and (b) comparison of vertical salinity difference, between observations and the model simulation.

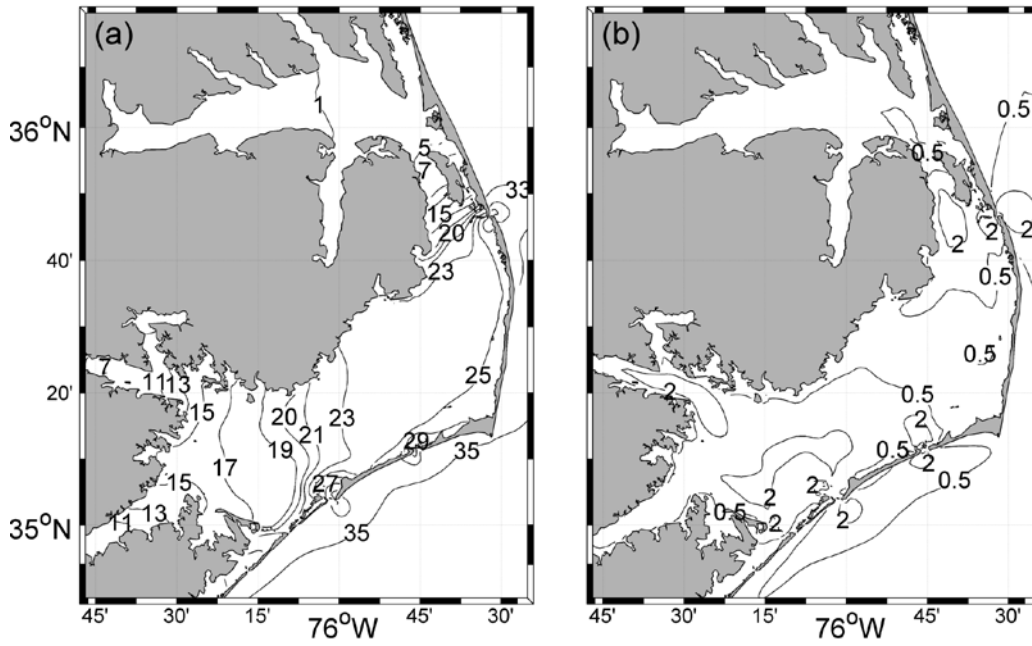


Figure 4.5 Distributions of mean (a) surface salinity, (b) vertical salinity difference two weeks before Hurricane Floyd.

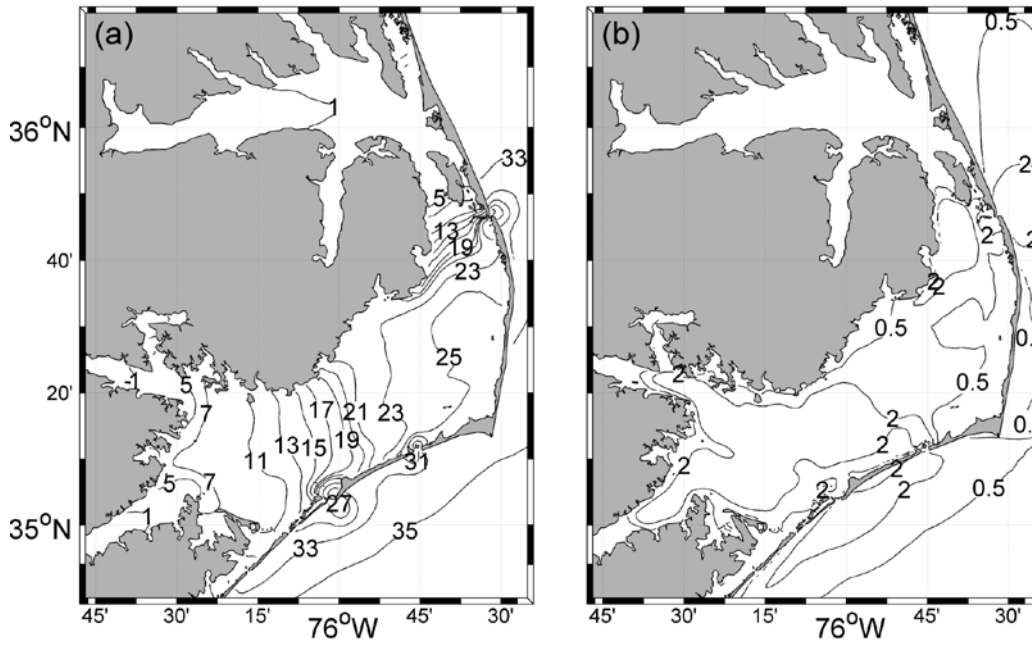


Figure 4.6 Distributions of mean (a) surface salinity, (b) vertical salinity difference in October 1999.

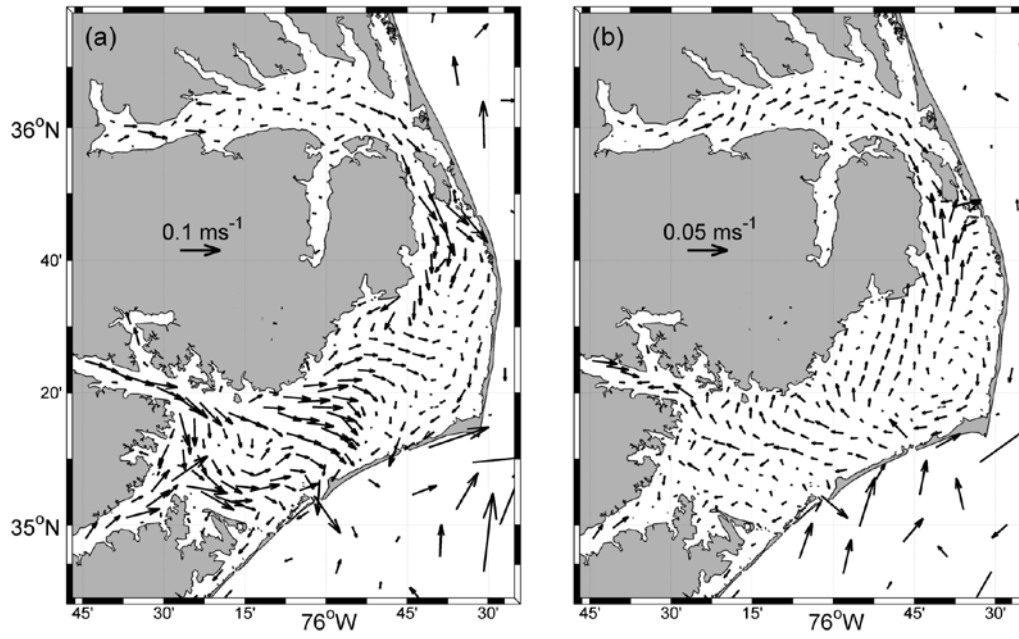


Figure 4.7 Distributions of mean (a) surface currents, (b) bottom currents in October 1999.

Chapter 5: Salt budget and salt balance

We have investigated the mean salinity distribution and mean circulation pattern in APS. The salinity in APS not only shows large spatial variations but also experiences large seasonal variations due to seasonal variations of the river discharges. Moreover, high-salinity water from the Atlantic Ocean enters APS through the inlets at the Outer Banks. In this section, we examine the salt budget in APS and analyze salt fluxes through the inlets.

APS receives freshwater from four rivers and exchanges salt with the Atlantic Ocean through the three inlets. The river discharges have a well-defined seasonal cycle: high flows during spring and low flows during summer. How do the river flows and salt fluxes through the inlets affect the seasonal evolution of salinity distribution in APS? Salt flux in an estuary can be decomposed into tidal pumping, subtidal shear dispersion and subtidal barotropic components. In long coastal-plain estuaries, subtidal vertical shear dispersion, resulting from the estuarine exchanges flow, is the dominant mechanism driving the salt flux (e.g. Lerczak and Geyer, 2006). However, tidal dispersion/pumping may dominate in regions of abrupt topographic changes such as headlands and inlets (Geyer and Signell, 1992). What are the relative importance of tidal pumping and shear-dispersion mechanisms in supplying salt to the lagoonal estuary? Wind-driven flows have been shown to be an important mechanism for the estuary-shelf exchange at the mouth of some estuaries (e.g. Valle-Levinson et al., 2001). What is the contribution of the wind-driven flows to the salt flux into APS?

5.1. Annual Salt Balance

Figure 5.1 shows the seasonal evolution of the surface salinity distribution in APS. During the winter month of February, salinity is high throughout APS, reaching over 23 psu in the central region of Pamlico Sound and 13 psu at the mouths of Neuse and Pamlico Rivers (Fig. 5.1a). High river discharges during the spring dramatically reduce the salinity in APS. Low-salinity water originated from Neuse and Pamlico Rivers spreads eastward and covers most of the southern Pamlico Sound, as shown by the location of 13-psu isohalines (May, Fig. 5.1b). Similarly, freshwater is pushed out of Albemarle Sound and enters the northern Pamlico Sound. Salinity in the central Pamlico Sound drops to 19 psu. In contrast, salinity shows a strong rebound over the summer: low-salinity water retreats to Neuse and Pamlico Rivers while high salinity (19 psu and higher) water occupies a large part of northern and central Pamlico Sound (August, Fig. 5.1c). During the fall, salinity shows relatively smaller changes: isohaline patterns around Neuse and Pamlico Rivers are almost the same while salinity in the central Pamlico Sound increases by about 2 psu (November, Fig. 5.1d).

We calculate the total salt content $M_s = \int S dV$ in APS where S is salinity and V the volume, and plot its temporal evolution in Fig. 5.2a. M_s averages to about 4×10^{11} psu m³ during Jan. and Feb. Due to large river discharges, the salt content decreases rapidly during the spring and reaches a minimum of 3×10^{11} psu m³. In contrast, M_s experiences substantial increases during the summer months and reaches a maximum of about 5×10^{11} psu m³ in early September. Runoff in early fall reduce M_s to 4×10^{11} psu m³. The salt content hovers around this value during the rest of year. Over the

course of 2003, the salt content in APS is about the same between the beginning and end of the year, even though it experiences large seasonal variations.

To understand how M_s changes over time, we integrate the salinity equation over the whole volume of APS and obtain

$$\frac{\partial M_s}{\partial t} = F_s \quad (5.1)$$

where F_s is the salt flux through the inlets given by

$$F_s = \langle \iint u S dA \rangle \quad (5.2)$$

in which the angle bracket represents a low-pass subtidal filter (with half-amplitude at 33 hours), u is axial velocity, S salinity, and A cross-sectional area. Figure 10b shows the total salt flux from all the inlets. We calculate the monthly averages of F_s to highlight seasonal variations of the salt flux. F_s is negative between February and April, indicating that salt is transported out of APS during the high runoff season. In contrast, F_s is positive over the summer (June – August), indicating that APS gains salt. We integrate F_s over time and find that its integral matches the total salt content M_s very well (see Fig. 5.2a).

To understand how various physical processes contribute to the salt flux through each inlet, we decompose the salt flux

$$\begin{aligned}
F_S &= \langle \iint (u_0 + u_E + u_T)(S_0 + S_E + S_T) dA \rangle \\
&\approx \langle \iint (u_0 S_0 + u_E S_E + u_T S_T) dA \rangle \\
&= F_0 + F_E + F_T
\end{aligned} \tag{5.3}$$

in which u and S are decomposed into tidally and cross-sectionally averaged (u_0, S_0), tidally averaged and cross-sectionally varying (u_E, S_E), and tidally and cross-sectionally varying (u_T, S_T) components, as in Lerczak et al. (2006). The first term F_0 is the salt flux due to subtidal cross-sectionally averaged transport, including the salt loss due to river discharge and subtidal salt flux fluctuations due to winds. Without wind forcing, $F_0 = -Q_f S_0$ is negative and equal to the product of the river discharge and oceanic salinity, but will be different if the wind-driven transport is important (Chen and Sanford, 2009). The second term F_E is the subtidal shear dispersion resulting from gravitational circulation. The third term F_T is the tidal oscillatory salt flux owing to temporal correlations between u_T and S_T . To aid the salt-flux analysis at the inlets, we will decompose the flow and density fields in APS into the subtidal and tidal components: the subtidal component is obtained by applying a 33-hour low-passed filter (Li et al., 2005) while the tidal component is the difference between the total and subtidal components.

Figure 5.3 shows the salt flux decomposition using Hatteras Inlet as an example. F_T is always positive so that tidal pumping supplies salt into APS. In a partially mixed estuary, F_E due to estuarine exchange flows is usually larger than tidally oscillatory flux F_T (Simpson et al., 2001; Lerczak et al., 2006). However, the baroclinic flow in the inlet is very weak such that F_E is nearly zero. In contrast, the barotropic subtidal

flux F_0 is much larger. The flows in Hatteras Inlet are predominantly barotropic. Pietradesa and Janowitz (1988) postulated and presented evidence that the flow through the narrow North Carolina barrier inlets, e.g. Oregon, Hatteras and Ocracoke Inlets, as being essentially bi-directional, i.e. either “in” or “out” throughout (Logan et al., 2000). Our analysis confirms their result. The subtidal barotropic salt flux F_0 is of either sign and shows large fluctuations at daily time scales. When averaged over the whole time period, however, F_0 is positive at Hatteras Inlet, indicating a net salt gain into APS.

Compared with the classic estuaries, the barotropic inlets are characterized by negligible salt flux due to exchange flow. In Fig.5.3, at the Hatteras Inlet, F_E is always positive but 100 times smaller compared with the other terms. Because of the very strong mixing generated by tidal currents, two-layer flow is rare. Vertically homogenous barotropic flow is dominant, so the dispersion of salt caused by vertical shear is very weak compared with the tidal dispersion.

5.2. Salt flux mechanisms

5.2.1. Tidal pumping

Temporal correlations between the currents and salinity at the tidal time scale lead to a net salt flux into APS. Figure 5.4 shows the time series of the tidal salt flux through Ocracoke, Hatteras and Oregon Inlets. For comparison, we plot the tidal sea-level time series at a nearby coastal station. Although tides are weak inside APS, tidal flows are strong inside the narrow inlets (Roelofs and Bumpus, 1953; Imasato et al.,

1994; Hench et al., 2002). F_T is weakest in Ocracoke Inlet and averages to about $0.4 \times 10^4 \text{ psu m}^3 \text{ s}^{-1}$. In contrast, F_T reaches a high mean value of $1.5 \times 10^4 \text{ psu m}^3 \text{ s}^{-1}$ in Oregon Inlet, due to stronger tidal flows there. The tidal salt flux through Hatteras Inlet falls to a middle ground, with the mean value of $0.75 \times 10^4 \text{ psu m}^3 \text{ s}^{-1}$. It is interesting to note that the tidal salt fluxes at the three inlets are generally higher during the spring tides than during the neap tides. The spring fluxes at Hatteras and Oregon Inlets are twice as large as the neap fluxes.

The tidal oscillatory salt flux F_T is due to the tidal pumping where flood–ebb asymmetries in the spatial structure of tidal currents near the inlet result in a net salt flux into the estuary, as originally proposed by Stommel and Farmer (1952) and discussed in Geyer and Signell (1992). We can examine the tidal pumping mechanism in more detail. Figure 5.5a shows that tidal velocity u_T and salinity S_T at Oregon Inlet are in-phase most of times over a tidal cycle. The net transport resulting from differences between the flood and ebb tidal currents leads to a salt flux into the estuary (Fig. 5.5b). In Figs. 5.5c and d, we show two snapshots of the current vector u_T and salinity S_T distributions near Oregon Inlet at the peak flood and ebb tide during the spring tide. The incoming flood tide creates a jet-like motion, injecting high-salinity water into APS. A semi-circular salinity/density front develops to separate the higher-salinity shelf water from the lower-salinity estuarine water. This density front propagates into the estuary during the flood phase of the tide. Since the tidal currents are strong, the salinity is nearly uniform behind the front. In comparison, the flow associated with the ebb tide is like a potential flow toward a sink, drawing low-

salinity estuarine waters from all directions to the inlet. Since Oregon Inlet is located close to Abermarle Sound, salinity increases from the northern side of Oregon Inlet to the southern side. Figures 5.5c and d reveals striking differences in the flow and density fields between the flood and ebb tides during the spring tide. A similar flood-ebb asymmetry is seen during the neap tide, although the tidal currents are weaker and the salinity difference between the flood and ebb tides are smaller. We have examined the momentum balance near the inlet and found a dominant balance between pressure gradient, horizontal advection and bottom stress, in agreement with the earlier studies of idealized and realistic inlets by Hench et al. (2002) and Hench and Luettich (2003).

Further insights into the tidal pumping mechanism can be gained by plotting the spatial distributions of depth-averaged horizontal salinity advection

$$F_{S_h} = \frac{1}{H} \int_{-H}^{\eta} \left(u \frac{\partial S}{\partial x} + v \frac{\partial S}{\partial y} \right) dz \quad \text{and vertical diffusive salt flux} \quad F_{S_v} = \frac{1}{H} \int_{-H}^{\eta} K_s \frac{\partial S}{\partial z} dz$$

near the inlet, as shown in Fig. 5.6. During the flood tide, F_{S_h} is mostly concentrated around the semi-circular salinity front whereas it is weak behind the front since the strong flood current homogenizes salinity there (Fig. 5.6c). Both vertical stratification and vertical diffusive salt flux drop to nearly zero (Figs. 5.6b and 5.6d). In contrast, the stratification and vertical diffusive salt flux are strong in the vicinity of the inlet during the ebb tide. Since the ebb current is relatively weak, the low-salinity estuarine water spreads over the more saline water that was injected into APS during the previous flood tide. Consequently, there is significant vertical diffusive flux acting on the stratified water. F_{S_h} during the ebb tide is distributed broadly but is weaker than

the flood tide. Over a flood-ebb tidal cycle, the volume-integrated horizontal salt advection $\iint_A HF_s h dA$, or equivalently the net salt flux through the control volume near the inlet, is larger during the flood phase than the ebb phase (Fig. 5.6a). The total salt gained during the flood phase $\int_0^{T/2} \iint_A HF_s h dAdt$ is 1.25×10^9 psu m^3 while the total salt lost during the ebb phase is -1.01×10^9 psu m^3 . Hence, the net gain of salt in the control volume due to tidal pumping is 2.40×10^8 psu m^3 . This compares with the net tidal salt gain of 5.88×10^8 psu m^3 through the cross-section at the inlet and shows that the remaining salt is pumped into the estuarine region outside the control volume.

5.2.2. Wind driven barotropic salt exchanges

Next we investigate the barotropic subtidal salt flux F_0 for the three inlets. As shown in Fig. 5.7, the short-term fluctuations in F_0 are due to barotropic transports across the inlets. The inlets have small surface areas so that local wind stress is not important. Instead the flows inside the inlets are driven by the sea-level difference/slope between APS and the adjacent shelf: the flows are directed into APS when the coastal sea level is higher than APS and vice versa (compare the 2nd and 3rd rows in Fig. 5.7). Let us take Oregon Inlet for an example. On day 312, the sea level is higher outside APS, the flow in the inlet is directed westward, and salt is supplied to APS from the adjacent Atlantic Ocean. On day 316, in contrast, the sea level is higher inside APS, the flow in the inlet is directed eastward, and salt is lost from APS. Due to the freshwater outflow from Albemarle Sound, the sea level is generally

higher on the APS side of Oregon Inlet such that salt is exported onto the shelf most of time. However, there are strong reversals of salt flux on day 255, 260, 312 when the sea level becomes higher on the shelf. The strong correlations between the time series of the sea-level difference, barotropic current and F_0 at all the three inlets demonstrate that the subtidal salt flux F_0 is carried by the subtidal barotropic flow driven by the sea-level slope across each inlet.

However, the sea-level height differences across the inlets do not bear simple correspondence with the wind speed, as shown in Figs. 5.7a-d. Winds modulate water levels on both sides of each inlet. Although wind-driven setup and set-down over a straight open shelf are easy to understand, the water level inside APS responds rapidly to wind forcing due to its shallowness and exhibits large spatial variations. Moreover, sea levels inside APS are affected by river discharges. For example, high river flows during the spring season raise the sea levels inside APS and promote outflows from the inlets. Sea levels also change at seasonal and longer time scales, due to thermal variability of the Atlantic Ocean (Roelofs and Bumpus, 1953; Pietrafesa et al., 1986) and shifts in the trajectory of the Gulf Stream (Blayo et al., 1996). Nevertheless, there are statistically significant correlations between the sea-level difference $\Delta\eta$ and wind speed components (U_{EW} in the east-west direction and U_{NS} in the south-north direction): the correlation coefficient r^2 between $\Delta\eta$ and U_{EW}/U_{NS} is 0.06/0.42, -0.57/0.26 and -0.49/-0.68 for Ocracoke, Hatteras and Oregon Inlets, respectively.

To better understand the subtidal salt flux F_0 through the inlets, we plot two snapshots of subtidal sea level, depth-averaged subtidal currents and subtidal salinity near the Oregon Inlet in Fig. 5.8. On day 312, the sea level is higher on the shelf than inside APS, driving a strong inflow through the inlet. Since the wind direction is southwestward, the incoming water moves southward inside APS, creating a large pocket of high-salinity water as shown in Fig. 5.8b. A salinity front separates this oceanic water from the lower-salinity estuarine water. This front looks similar to the salinity/density front seen during the flood tides, but its area extent is much larger (compare Fig. 5.8b with Figs. 5.5c or 5.5e) since the wind-driven subtidal current lasts much longer than the half of the tidal period. On day 316, the sea level is higher inside APS than on the shelf, driving a strong outflow through Oregon Inlet. The wind is northeastward and drives the plume on the shelf in the same direction. Inside APS, convergent flows carry low-salinity estuarine water towards the inlet. Again there is a salinity gradient in the north-south direction due to the presence of fresh water in Albemarle Sound in the north.

We analyze the depth-integrated momentum budget near Oregon Inlet during both days and find a primary balance between pressure gradient, horizontal advection and bottom stress, as shown in Fig. 5.9. On day 312, the pressure gradient is directed eastward since the sea level is higher on the shelf than inside APS. This drives an eastward inflow through the inlet so that the bottom stress is directed westward. The dominant advection term is $-u \frac{\partial u}{\partial x}$ (moved to the right-hand side) in the along-inlet

direction: outside the inlet, u is negative (westward) and $\frac{\partial u}{\partial x}$ is positive (convergent flows) such that $-u \frac{\partial u}{\partial x} > 0$; inside the inlet, u is still negative but $\frac{\partial u}{\partial x}$ becomes negative (divergent flows) such that $-u \frac{\partial u}{\partial x} < 0$. We find a similar result in the momentum balance on day 315. The eastward-directed pressure gradient due to sea-level slope drives an outflow and is balanced by the westward bottom stress. At first it may appear surprising that the advection term has the same distributions of directions/signs as on day 312 even though the flow through the inlet is reversed.

Inside the inlet, $u > 0$ and $\frac{\partial u}{\partial x} > 0$ (convergent flows) such that $-u \frac{\partial u}{\partial x} < 0$. Outside the inlet, $u > 0$ and $\frac{\partial u}{\partial x} < 0$ (divergent flows) such that $-u \frac{\partial u}{\partial x} > 0$. These results on the momentum balance for the subtidal wind-driven flows are similar to those on the tidal flows through the inlets (Hench et al., 2002; Hench and Luettich, 2003). As the inlet is approached, the pressure gradient drives flow acceleration with the remainder balanced by the bottom friction. As the flow leaves the inlet, the bottom stress decelerates the current as well as balances the pressure gradient. Finally, we note that there are striking similarities in the flow patterns and salt fluxes between the tidal and subtidal/wind-driven flows (see Figs. 5.5 and 5.8).

In the above analysis, we decompose the current and salinity fields into tidal and subtidal components. One might question if the tidal salt flux F_T is influenced by the subtidal wind-driven currents or whether the subtidal barotropic salt flux F_0 is

influenced by the tidal currents. We have examined the correlation between u_0 and u_T and found the correlation coefficient to be about 2% in all three inlets. We have also examined the correlation between u_0 and $\Delta\eta_T$, and again found the correlation coefficient to be about 2% in the three inlets. This compares with a high correlation coefficient between u_0 and $\Delta\eta_0$, which is 0.78, 0.94 and 0.97 for Ocracoke, Hatteras and Oregon Inlets, respectively. Therefore, the salt flux decomposition shown in (3) is valid.

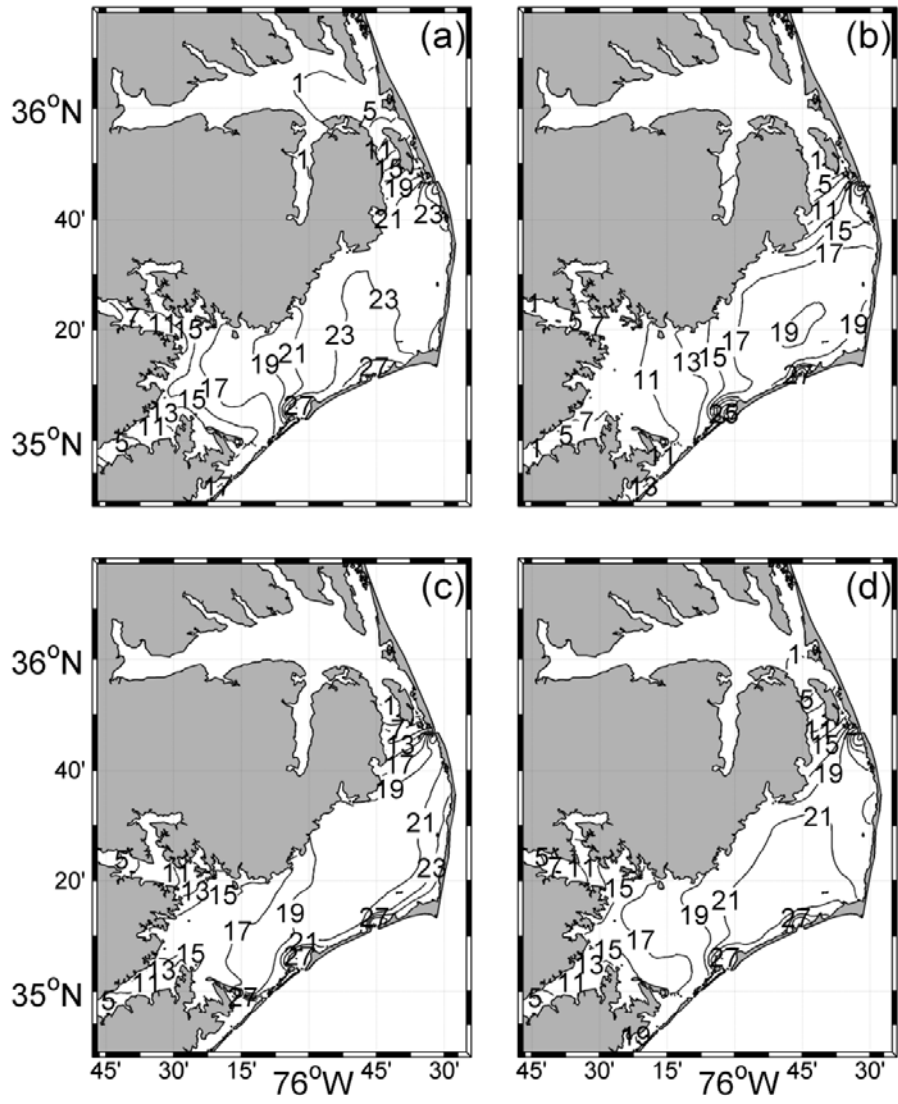


Figure 5.1 Monthly mean surface salinity distributions in (a) February, (b) May, (c) August, and (d) November.

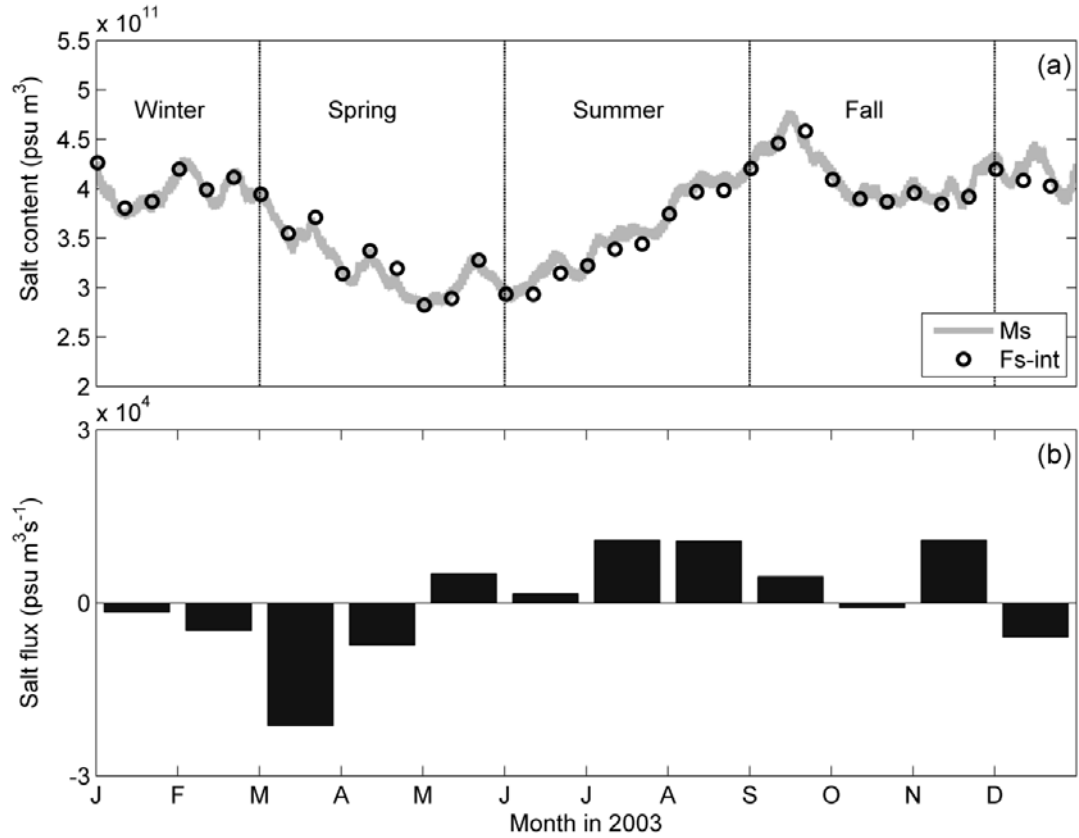


Figure 5.2 (a) Time series of total salt content in APS (thick grey line) and integrated salt flux through all inlets (open circles). (b) Monthly averages of total salt flux through the inlets.

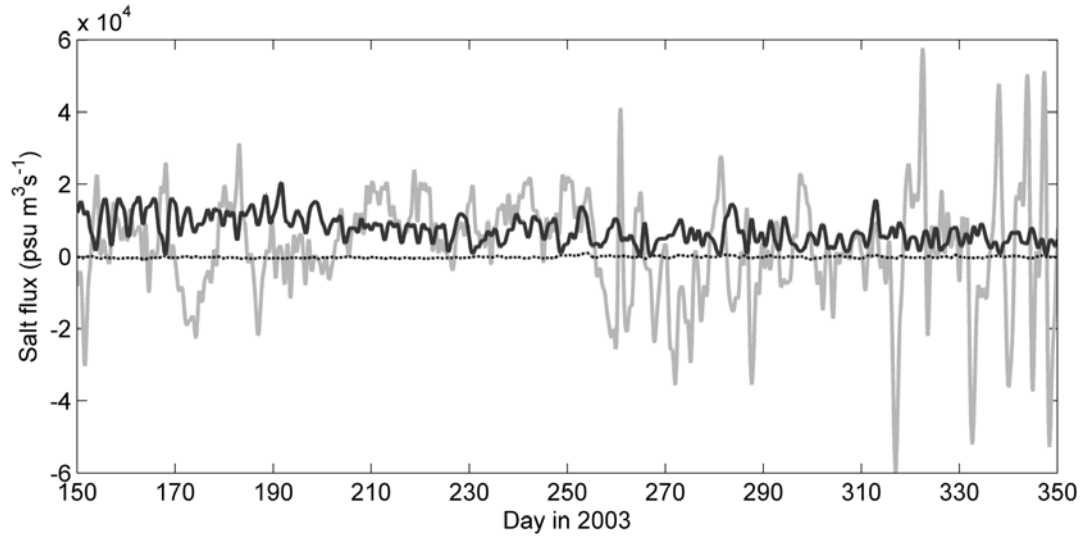


Figure 5.3 Salt flux decomposition at Hatteras Inlet: shear dispersion due to baroclinic exchange flow F_E (dashed line), tidal pumping F_T (black line), and wind-driven barotropic transport F_0 (grey line).

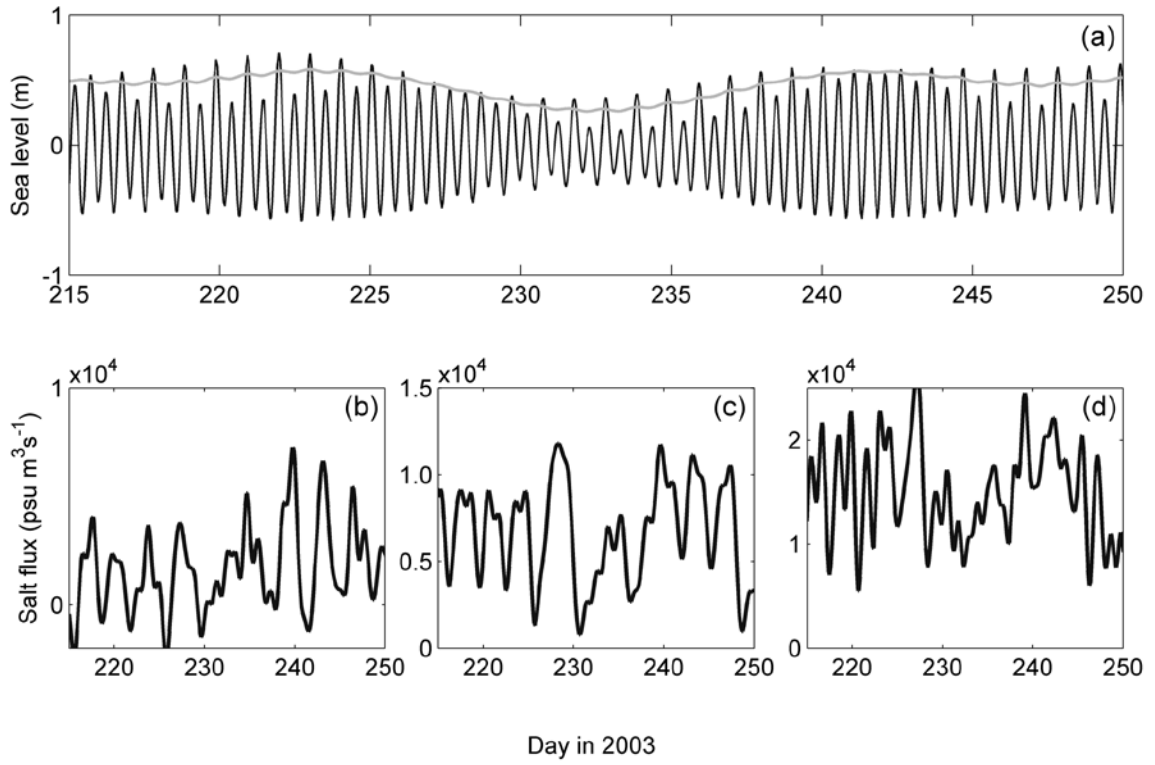


Figure 5.4 (a) Time series of sea level at Duck tidal gauge station. Time series of F_T at (b) Ocracoke, (c) Hatteras, and (d) Oregon Inlet.

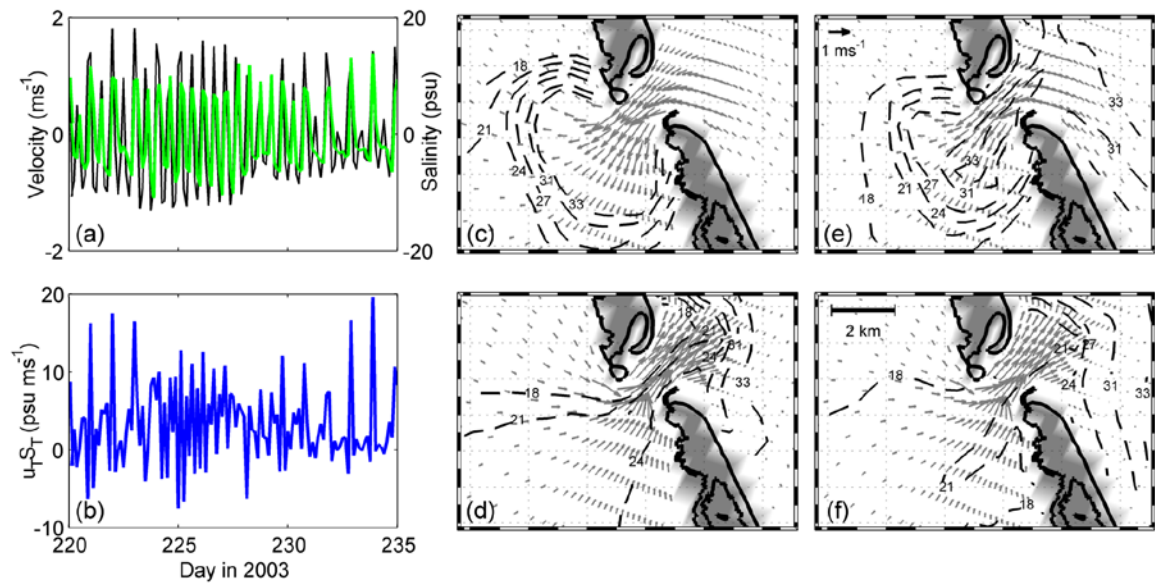


Figure 5.5 Time series of (a) tidal velocity (black) and tidal salinity (green), and (b) the product of tidal velocity and tidal salinity (blue) at Oregon Inlet. Snapshots of depth-averaged velocity (vectors) and salinity (contours) distributions near Oregon Inlet on (c)/(e) peak flood (day 222/229.75) and (d)/(f) peak ebb (day 222.25/230) during the spring/neap tide. The shaded areas are discretized model representations of Outer Banks while the thick solid lines are high-resolution coastlines obtained from NOAA.

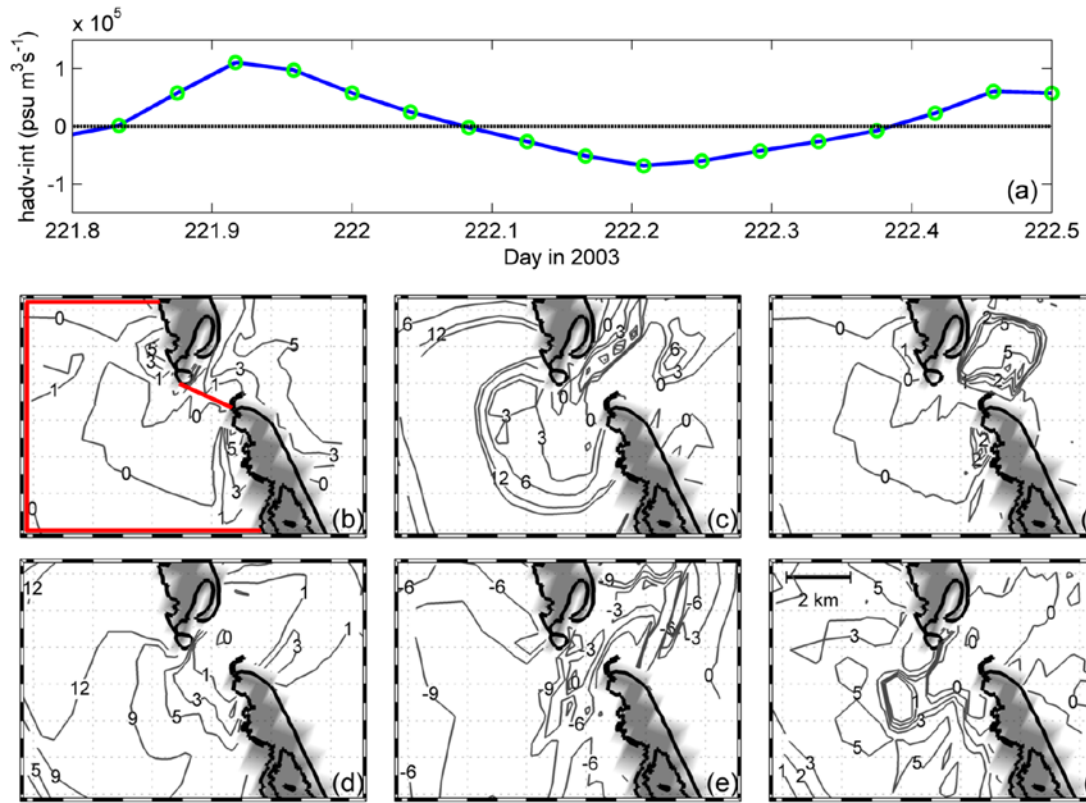


Figure 5.6 Time series of (a) integrated horizontal advection in the control volume [defined as the quadrilateral marked by red lines in (b)]. Distributions of (b)/(d) vertical salinity difference, (c)/(e) depth-averaged horizontal salinity advection term (in $10^{-4} \text{ psu s}^{-1}$), and (d)/(f) depth-averaged vertical diffusion term (in $10^{-3} \text{ psu ms}^{-1}$) on day 222 (flood) and 222.25 (ebb).

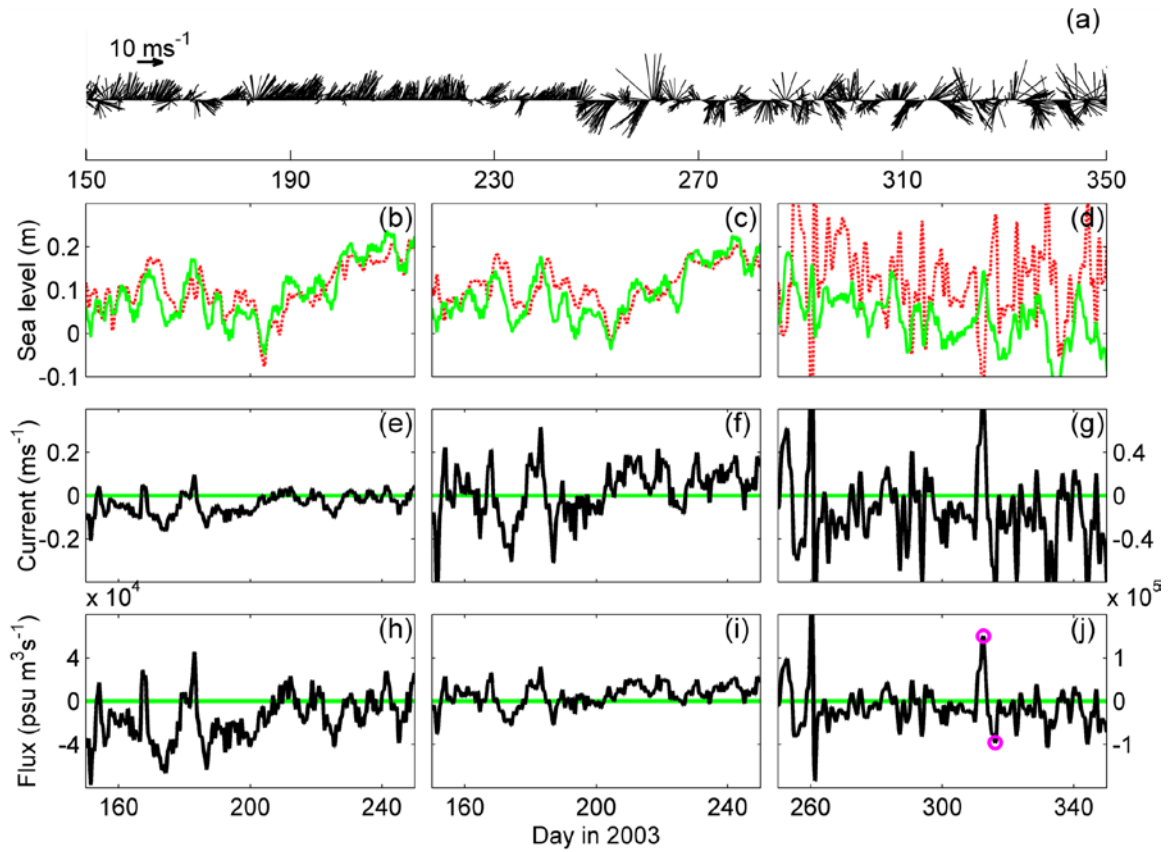


Figure 5.7 (a) Wind speed vectors at Cape Hatteras. Time series of subtidal sea levels across (b) Ocracoke, (c) Hatteras, and (d) Oregon Inlet: red dashed lines correspond to stations inside APS and green lines to stations outside APS. Time series of the sectionally averaged barotropic current at (e) Ocracoke, (f) Hatteras and (g) Oregon Inlet. Time series of barotropic salt flux F_0 at (h) Ocracoke, (i) Hatteras and (j) Oregon Inlet. The two days marked in magenta open circles are used in the subsequent analysis.

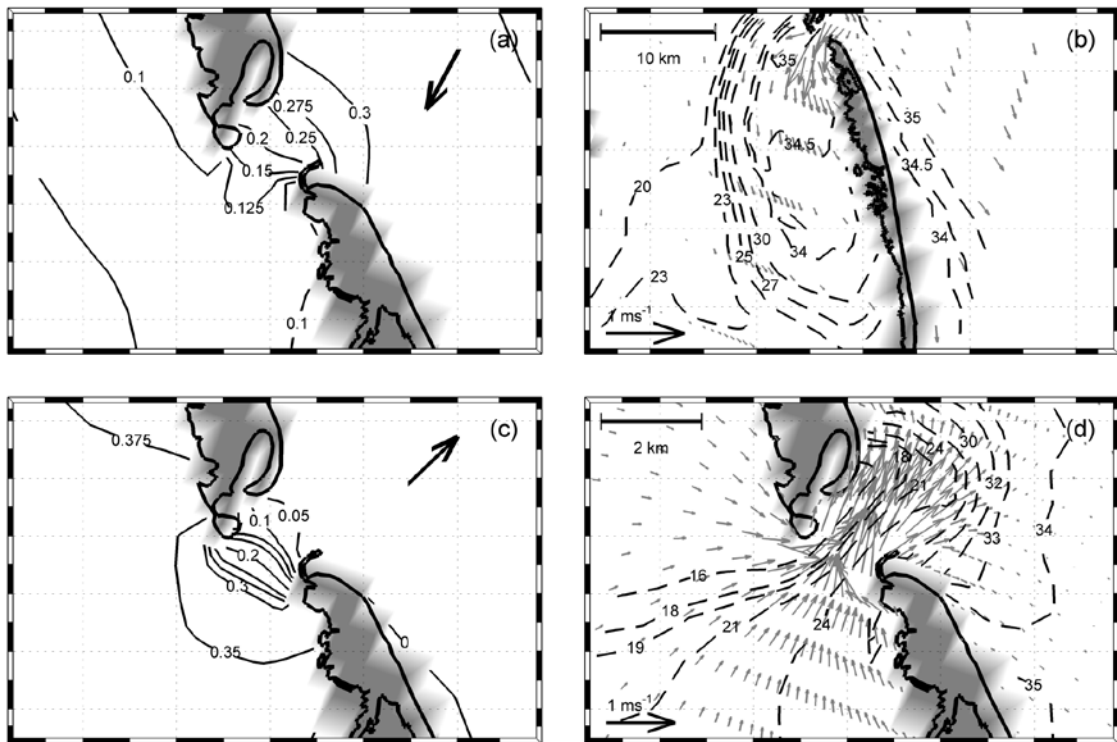


Figure 5.8 Distributions of (a)/(c) subtidal sea level and (b)/(d) depth-averaged subtidal currents (arrows) and salinity (contours) near Oregon Inlet on day 312.5/316.125. Solid arrows in (a) and (c) indicate the wind directions.

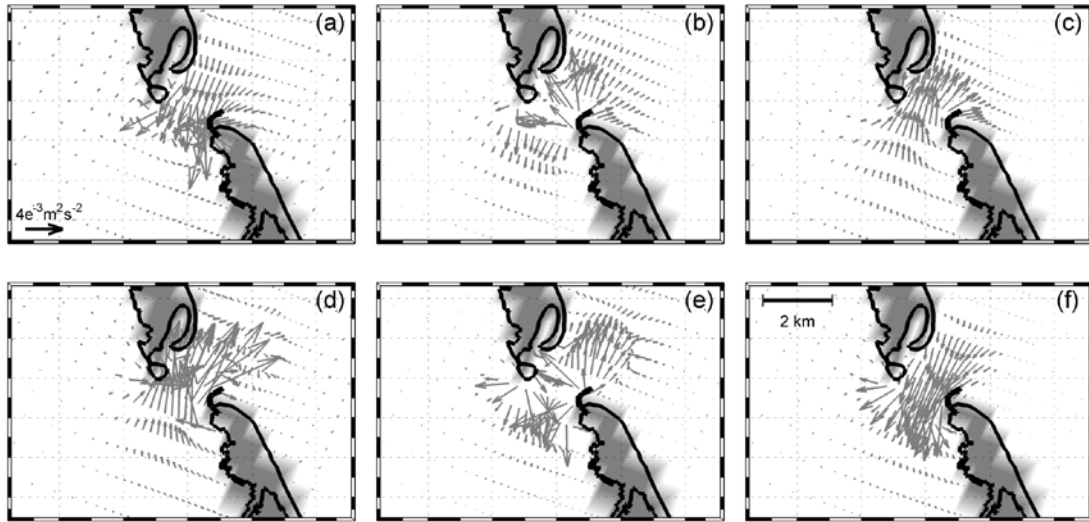


Figure 5.9 Horizontal distributions of (a)/(d) pressure gradient, (b)/(e) horizontal advection, (c)/(f) bottom stress near Oregon Inlet on day 312.5/316.125.

Chapter 6: Final conclusion

We have employed ROMS to develop a new 3D hydrodynamic model for APS and used it to investigate the circulation dynamics, stratification variations and salt balance in this lagoonal estuary. Although the vertical stratification is weak, the geographic separation between the rivers and inlets generates large horizontal density gradients. The mean circulation features a two-layer gravitational circulation with speeds reaching several cm s^{-1} : the fresh surface waters leave the rivers and the saline bottom waters leave the inlets. Analysis of the depth-integrated momentum budget shows a primary balance between the barotropic pressure gradient due to sea-level slope and the baroclinic pressure gradient due to horizontal salinity gradients. The wind stress is not a major driver of the mean circulation. In our view, this is a significant result and demonstrates that substantial gravitational circulation can develop in shallow, wide and weakly stratified lagoonal estuaries. This two-layer mean circulation can play an important role in transporting nutrients, contaminants and fish larvae in these estuarine systems (Paerl et al., 1998; Werner and Brain, 1999).

Because of their layouts, the flow responses of three separated regions to the same wind are very different, depending on the relative importance of wind stress compared with horizontal salinity gradient. Using idealized wind stress, we introduced Wedderburn number and Csanady linear solution to explain the wind's effects. Using year 2003 as an example, we conducted hindcast simulations. The seasonal circulation is driven by seasonally shifting prevailing winds but is also

affected by the horizontal density gradients. The typical current response to the wind forcing in the Pamlico southern basin is a two-layer baroclinic flow as the winds generate the sea-level slope and pressure gradient which work against the wind stress, although the winds generate down-wind currents at all depths in shallow shoals in the Pamlico northern basin and Albemarle Sound. Both flow pattern and momentum balance show very good agreement between the idealized cases and realistic simulation in two seasons (summer and winter), which confirms that the seasonal circulation is driven by seasonally shifting prevailing winds.

Due to seasonal variations of river discharges, salinity distributions in APS show strong seasonal variations. The salt content in APS is determined by the balance between the river flows and salt exchanges through the inlets. We analyzed the salt flux decomposition to gain insights into the physical mechanisms controlling the salt exchanges through the inlets. While the salt flux due to estuarine exchange flows is weak, tidal pumping produces a net influx of salt into APS over a tidal cycle: strong flood currents push high-salinity oceanic water into the estuary through a propagating density front whereas convergent ebb currents advect lighter estuarine water over denser bottom water. The salt flux due to barotropic transport across the inlets shows large temporal fluctuations and can either be a source or sink of salt to APS. This salt flux component correlates well with the sea level difference across each inlet. The salt flux F_T due to the tidal pumping averages to 3.3×10^4 psu $\text{m}^3 \text{s}^{-1}$. The subtidal barotropic salt flux F_0 consists of the salt loss due to river discharge and subtidal salt flux fluctuations due to wind-driven exchanges across the inlets. F_0 averages to

-5.2×10^4 psu m^3s^{-1} during the spring and to -2.7×10^4 psu m^3s^{-1} during the summer. In comparison, the subtidal salt flux F_E due to shear dispersion is much smaller: a mean value of 28.8 psu m^3s^{-1} for spring and a mean value of 296 psu m^3s^{-1} for summer. Therefore, the seasonal change of the salt content in APS is primarily determined by the balance between F_T and F_0 . However, it is impossible to separate the relative contributions of river discharge and wind-driven transports to F_0 because there is an interconnected network of 4 rivers and 3 inlets in APS.

The hydrodynamic model developed here could provide a useful tool for investigating how climatic variability and extreme weather events affect plankton productivity and water quality in APS. The fresh water from the rivers carries various forms of nutrients, organic matter, and toxic materials to APS. The combination of the hydrological and nutrient cycling characteristics makes it highly susceptible to nutrient inputs, leading to algal blooms, hypoxia, and anoxia. River discharge, winds and stratification have been recognized as the leading physical processes affecting the plankton system in APS (Paerl et al., 2001; Paerl et al., 2006a). Climatic perturbations by drought-flood cycles, tropical storms, and hurricanes are increasingly important in Mid-Atlantic estuaries such as APS. A biogeochemical model coupled to the hydrodynamic model developed here can be used to investigate the impact of climate variability/change on the plankton productivity in APS.

Bibliography

- Blayo, E., J. Verron, J. Molines, and L. Testard (1996), Monitoring of the Gulf Stream path using Geosat and Topex/Poseidon altimetric data assimilated into a model of ocean circulation, *J. Marine Syst.*, 8(1-2), 73-89.
- Buzzelli, C., J. Ramus, and H. Paerl (2003), Ferry-based monitoring of surface water quality in North Carolina estuaries, *Estuaries Coasts*, 26(4), 975-984.
- Carton, J., G. Chepurin, X. Cao, and B. Giese (2000), A Simple Ocean Data Assimilation analysis of the global upper ocean 1950-1995, Part 1: methodology, *J. Phys. Oceanogr.*, 30, 294-309.
- Carton, J., G. Chepurin, and X. Cao (2000), A simple ocean data assimilation analysis of the global upper ocean 1950-95. Part II: Results, *J. Phys. Oceanogr.*, 30(2), 311-326.
- Chen, S., and L. Sanford (2009), Axial wind effects on stratification and longitudinal salt transport in an idealized, partially mixed estuary, *J. Phys. Oceanogr.*, 39(8), 1905-1920.
- Churchill, J. H., J. L. Hench, R. A. Luettich, J. O. Blanton, and F. E. Werner (1999), Flood tide circulation near Beaufort Inlet, North Carolina: implications for larval recruitment, *Estuaries Coasts*, 22(4), 1057-1070.
- Cromwell, J. (1973), Barrier coast distribution: a world-wide survey, *Barrier Islands*, 407-408.
- Egbert, G., A. Bennett, and M. Foreman (1994), TOPEX/POSEIDON tides estimated using a global inverse model, *J. Geophys. Res.*, 99(C12), 24821.
- Egbert, G., and S. Erofeeva (2002), Efficient inverse modeling of barotropic ocean tides, *J. Atmos. Oceanic Technol.*, 19(2), 183-204.
- Fairall, C. W., E. F. Bradley, J. E. Hare, A. A. Grachev, and J. B. Edson (2003), Bulk parameterization of air-sea fluxes: updates and verification for the COARE algorithm, *J. Climate*, 16(4), 571-591.
- Geyer, W., and R. Signell (1992), A reassessment of the role of tidal dispersion in estuaries and bays, *Estuaries Coasts*, 15(2), 97-108.
- Geyer, W., J. Trowbridge, and M. Bowen (2000), The dynamics of a partially mixed estuary, *J. Phys. Oceanogr.*, 30(8), 2035-2048.

- Haidvogel, D., H. Arango, K. Hedstrom, A. Beckmann, P. Malanotte-Rizzoli, and A. Shchepetkin (2000), Model evaluation experiments in the North Atlantic Basin: simulations in nonlinear terrain-following coordinates, *Dynam. Atmos. Oceans*, 32(3-4), 239-281.
- Hench, J., B. Blanton, and R. Luettich (2002), Lateral dynamic analysis and classification of barotropic tidal inlets, *Cont. Shelf Res.*, 22(18-19), 2615-2631.
- Hench, J., and R. Luettich Jr (2003), Transient tidal circulation and momentum balances at a shallow inlet, *J. Phys. Oceanogr.*, 33(4), 913-932.
- Huang, W., H. Sun, S. Nnaji, and W. Jones (2002), Tidal hydrodynamics in a multiple-inlet estuary: Apalachicola Bay, Florida, *J. Coastal Res.*, 18(4), 674-684.
- Imasato, N., S. Fujio, Q. Zhang, T. Awaji, and K. Akitomo (1994), Three-dimensional numerical experiments on tidal exchange through a narrow strait in a homogeneous and a stratified sea, *J. Oceanogr.*, 50(2), 119-139.
- Jay, D., and J. Smith (1990), Circulation, density distribution and neap-spring transitions in the Columbia River Estuary, *Prog. Oceanogr.*, 25(1-4), 81-112.
- Lerczak, J., and W. Geyer (2004), Modeling the lateral circulation in straight, stratified estuaries, *J. Phys. Oceanogr.*, 34, 1410-1428.
- Lerczak, J., W. Geyer, and R. Chant (2006), Mechanisms driving the time-dependent salt flux in a partially stratified estuary, *J. Phys. Oceanogr.*, 36(12), 2296-2311.
- Levitus, S. (1982), *Climatological atlas of the world ocean*, United States Government Printing.
- Li, M., L. Zhong, and W. Boicourt (2005), Simulations of Chesapeake Bay estuary: Sensitivity to turbulence mixing parameterizations and comparison with observations, *J. Geophys. Res.*, 110, C12004.
- Li, M., and L. Zhong (2009), Flood-ebb and spring-neap variations of mixing, stratification and circulation in Chesapeake Bay, *Cont. Shelf Res.*, 29(1), 4-14.
- Lin, J., L. Xie, L. Pietrafesa, J. Ramus, and H. Paerl (2007), Water quality gradients across Albemarle-Pamlico estuarine system: seasonal variations and model applications, *J. Coastal Res.*, 23(1), 213-229.
- Logan, D., J. Morrison, L. Pietrafesa, T. Hopkins, and J. Churchill (2000), Physical oceanographic processes affecting inflow/outflow through Beaufort Inlet, North Carolina, *J. Coastal Res.*, 16(4), 1111-1125.

- Luettich, R., L. James, F. E. Werner, and O. Brian (1999), Barotropic tidal and wind driven larval transport in the vicinity of a barrier island inlet, *Fisheries Oceanography*, 8, 190-209.
- Luettich, R., S. Carr, J. Reynolds-Fleming, C. Fulcher, and J. McNinch (2002), Semi-diurnal seiching in a shallow, micro-tidal lagoonal estuary, *Cont. Shelf Res.*, 22(11-13), 1669-1681.
- MacCready, P., N. Banas, B. Hickey, E. Dever, and Y. Liu (2009), A model study of tide-and wind-induced mixing in the Columbia River estuary and plume, *Cont. Shelf Res.*, 29(1), 278-291.
- MacCready, P., and W. Geyer (2010), Advances in estuarine physics, *Ann. Rev. Mar. Sci.*, 2, 35-58.
- Marchesiello, P., J. McWilliams, and A. Shchepetkin (2001), Open boundary conditions for long-term integration of regional oceanic models, *Ocean Modell.*, 3(1-2), 1-20.
- Mesinger, F., G. DiMego, E. Kalnay, K. Mitchell, P. Shafran, W. Ebisuzaki, D. Jovic, J. Woollen, E. Rogers, and E. Berbery (2006), North American regional reanalysis, *Bull. Am. Meteorol. Soc.*, 87(3), 343-360.
- Noble, M., W. Schroeder, W. Wiseman Jr, H. Ryan, and G. Gelfenbaum (1996), Subtidal circulation patterns in a shallow, highly stratified estuary: Mobile Bay, Alabama, *J. Geophys. Res.*, 101(C11), 25689.
- Paerl, H., J. L. Pinckney, J. M. Fear, and B. L. Peierls (1998), Ecosystem responses to internal and watershed organic matter loading: consequences for hypoxia in the eutrophying Neuse River Estuary, North Carolina, USA, *Mar. Ecol. Prog. Ser.*, 166, 17-25.
- Paerl, H., J. Bales, L. Ausley, C. Buzzelli, L. Crowder, L. Eby, J. Fear, M. Go, B. Peierls, and T. Richardson (2001), Ecosystem impacts of three sequential hurricanes (Dennis, Floyd, and Irene) on the United States' largest lagoonal estuary, Pamlico Sound, NC, *Proc. Natl. Acad. Sci. U.S.A.*, 98(10), 5655.
- Paerl, H. W., L. M. Valdes, B. L. Peierls, J. E. Adolf, and L. W. Harding Jr (2006), Anthropogenic and climatic influences on the eutrophication of large estuarine ecosystems, *Limnol. Oceanogr.*, 51(1), 448-462.
- Paerl, H., K. Rossignol, R. Guajardo, N. Hall, A. Joyner, B. Peierls, and J. Ramus (2009), FerryMon: Ferry-Based Monitoring and Assessment of Human and Climatically Driven Environmental Change in the Albemarle-Pamlico Sound System, *Environ. Sci. Technol.*, 43(20), 7609-7613.

- Peters, H. (1999), Spatial and temporal variability of turbulent mixing in an estuary, *J. Mar. Res.*, 57(6), 805-845.
- Pietrafesa, L. J., G. S. Janowitz, T.-Y. Chao, R. H. Weisberg, F. Askari, and E. Nobel (1986), The physical oceanography of Pamlico Sound, UNC Sea Grant Publication UNC-SG-WP-86-5.
- Pietrafesa, L. J., and G. S. Janowitz (1988), Physical oceanographic processes affecting larval transport around and through North Carolina inlets, *Larval fish and shellfish transport through inlets*, 3, 34-50.
- Pritchard, D. W. (1955), Estuarine circulation patterns, *Proc. Am. Soc. Civ. Eng.*, 81 (717), 1 - 11.
- Pritchard, D. W. (1956), The dynamic structure of a coastal plain estuary, *J. Mar. Res.*, 15(33-42).
- Ralston, D.K., W.R. Geyer, and J.A. Lerczak (2008). Subtidal salinity and velocity in the Hudson River estuary: observations and modeling, *J. Phys. Oceanogr.*, 38, 753-770.
- Reyns, N., D. Eggleston, and R. Luettich Jr (2006), Secondary dispersal of early juvenile blue crabs within a wind-driven estuary, *Limnol. Oceanogr.*, 51(5), 1982-1995.
- Roelofs, E., and D. Bumpus (1953), The hydrography of Pamlico Sound, *Bull. Mar. Sci.*, 3(3), 181-205.
- Savidge, D., and J. Bane Jr (2001), Wind and Gulf Stream influences on along-shelf transport and off-shelf export at Cape Hatteras, North Carolina, *J. Geophys. Res.*, 106(C6), 11505.
- Scully, M., W. Geyer, and J. Lerczak (2009), The influence of lateral advection on the residual estuarine circulation: A numerical modeling study of the Hudson River estuary, *J. Phys. Oceanogr.*, 39(1), 107-124.
- Simpson, J., R. Vennell, and A. Souza (2001), The salt fluxes in a tidally-energetic estuary, *Estuarine Coastal Shelf Sci.*, 52(1), 131-142.
- Smith, N. (2001), Seasonal-scale transport patterns in a multi-inlet coastal lagoon, *Estuarine Coastal Shelf Sci.*, 52(1), 15-28.
- Song, Y., and D. Haidvogel (1994), A semi-implicit ocean circulation model using a generalized topography-following coordinate system, *J. Comput. Phys.*, 115(1), 228-244.

- Stommel, H., and H. Farmer (1952), On the nature of estuarine circulation. *Rep.*, Woods Hole Oceanographic Institute Technical Report.
- Sutherland, D., P. MacCready, N. Banas, and L. Smedstad (2010), A model study of the Salish Sea estuarine circulation, *J. Phys. Oceanogr.*, *Submitted*.
- Valle-Levinson, A., K. Wong, and K. Lwiza (2000), Fortnightly variability in the transverse dynamics of a coastal plain estuary, *J. Geophys. Res.*, *105(C2)*, 3413-3424.
- Valle-Levinson, K. Wong, and K. T. Bosley (2001), Observations of the wind-induced exchange at the entrance to Chesapeake Bay, *J. Mar. Res.*, *59*, 391-416.
- Warner, J., W. Geyer, and J. Lerczak (2005), Numerical modeling of an estuary: A comprehensive skill assessment, *J. Geophys. Res.*, *110(C5)*, C05001.
- Warner, J., C. Sherwood, H. Arango, and R. Signell (2005), Performance of four turbulence closure models implemented using a generic length scale method, *Ocean Modell.*, *8(1-2)*, 81-113.
- Werner, F., J. Blanton, D. Lynch, and D. Savidge (1993), A numerical study of the continental shelf circulation of the US South Atlantic Bight during the autumn of 1987, *Cont. Shelf Res.*, *13(8-9)*, 971-997.
- Werner, F., and O. Brain (1999), Physical oceanography of the North Carolina continental shelf during the fall and winter seasons: implications for the transport of larval menhaden, *Fisheries Oceanography*, *8*, 7-21.
- Wong, K. (1991), The effect of coastal sea level forcing on Indian River Bay and Rehoboth Bay, Delaware, *Estuarine Coastal Shelf Sci.*, *32(3)*, 213-229.
- Xie, L., and L. Pietrafesa (1999), Systemwide Modeling of Wind and Density Driven Circulation in Croatan-Albemarle-Pamlico Estuary System Part I: Model Configuration and Testing, *J. Coastal Res.*, *15(4)*, 1163-1177.
- Xie, L., and D. Eggleston (1999), Computer simulations of wind-induced estuarine circulation patterns and estuary-shelf exchange processes: the potential role of wind forcing on larval transport, *Estuarine Coastal Shelf Sci.*, *49(2)*, 221-234.
- Xu, H., J. Lin, and D. Wang (2008), Numerical study on salinity stratification in the Pamlico River Estuary, *Estuarine Coastal Shelf Sci.*, *80(1)*, 74-84.